

Coercive Field Reduction in Ultra-thin $\text{Al}_{1-x}\text{Sc}_x\text{N}$ via Interfacial Engineering with a Scandium Electrode

AUTHOR NAMES Yinuo Zhang,¹ Rajeev Kumar Rai,² Giovanni Esteves,³ Yubo Wang,¹ Deep
M. Jariwala,¹ Eric A. Stach^{2,*} and Roy H. Olsson, III^{1,*}

AUTHOR ADDRESS

1. Department of Electrical and Systems Engineering, University of Pennsylvania,
Philadelphia, PA, USA 19104
2. Department of Materials Science and Engineering, University of Pennsylvania,
Philadelphia, PA, USA 19104
3. Microsystems Engineering, Science and Applications (MESA) Center, Sandia National
Laboratories, Albuquerque, NM, USA 87185

* Corresponding Authors: stach@seas.upenn.edu, rolsson@seas.upenn.edu

KEYWORDS: Ferroelectrics, Ultra-thin Films, $\text{Al}_{1-x}\text{Sc}_x\text{N}$, Interfacial Engineering, Ferroelectric
Memory, Strain Mapping, XRD

ABSTRACT

Aluminum scandium nitride (AlScN) ferroelectrics are promising for next-generation non-volatile memory applications due to high remnant polarization compared with $\text{Pb}(\text{Zr}_x\text{Ti}_{1-x})\text{O}_3$ and doped- HfO_2 material systems, as well as their fast switching and scalability to nanometer thicknesses. As device dimensions shrink, the coercive field in ultra-thin ferroelectric films increases, which challenges low-voltage operation. We demonstrate that interfacial engineering through bottom electrode selection and strain management reduces this coercive field increase with scaling and improves ferroelectric performance. Here, we demonstrate robust ferroelectricity in ultra-thin AlScN capacitors deposited on a Sc bottom electrode under both alternating current and direct current conditions. The coercive field is reduced by over 20% compared to capacitors with an Al bottom electrode. Furthermore, the difference in dynamic switching behavior was evaluated by applying the Kolmogorov–Avrami–Ishibashi (KAI) model. At low frequencies (<16.7 kHz), the capacitors with Sc and Al bottom electrodes exhibit comparable KAI exponents (0.036 and 0.028, respectively), indicating similar switching kinetics. However, at higher frequencies, the capacitor with an Al bottom electrode shows a significantly higher exponent (0.093), indicating a stronger frequency dependence, whereas the capacitor with a Sc bottom electrode maintains a stable exponent of 0.036, suggesting a lower frequency dependence during faster switching scenarios. The Scanning Electron Nanobeam Diffraction technique was selected to measure the strain difference in AlScN thin films grown on templates with different lattice mismatch, providing a correlation between lattice mismatch, film strain and switching behavior in ultra-thin film systems.

INTRODUCTION:

Recently, the Sc-alloyed AlN film system has attracted significant interest as a component in next-generation electronics, due to its unique and tunable properties, including ferroelectricity and piezoelectricity.¹⁻⁴ Due to its large remnant polarization (P_r), low permittivity, and stable wurtzite structure at high temperatures compared to traditional ferroelectric materials,⁵⁻⁸ the AlScN system has potential applications in non-volatile memory (NVM) technology, including ferroelectric random-access memory (FeRAM) and ferroelectric field-effect transistors (FE-FETs).⁹⁻¹⁴ Notably, AlScN film thickness can be reduced to sub-5 nm dimensions and retain ferroelectricity.^{15, 16} AlScN is also compatible with Back-End-of-Line (BEOL) Complementary Metal-Oxide-Semiconductor (CMOS) manufacturing.^{17, 18} These two features indicate that it can be a key component of multiple third-generation semiconductor commercial applications.^{1, 15, 19, 20} Reducing the coercive field to achieve polarization switching will lead to faster switching speed and lower energy consumption, improving the performance of AlScN-based memory devices. Strain engineering has been demonstrated as an effective approach for tailoring the functionality and enhancing the performance of thin films across a range of applications.²¹⁻²⁴ Epitaxial strain at the film interface arises from lattice constant mismatch between the film and the growth substrate.²⁵⁻²⁷ This strain can cause crystalline distortions or defect formation that significantly impacts the crystallinity, grain structure, and electronic properties of semiconductor materials.²⁸ In ferroelectric materials, strain engineering at the interface enables precise modulation of domain structure and key physical properties, including dielectric constants and leakage currents, offering a powerful strategy for tailoring material performance.^{28, 29}

In the AlScN system, compressive strain is expected to increase the coercive field (E_C) and thus raise the switching energy of memory devices.^{4, 30} Increases in the c/a ratio close to the interface

would therefore be expected to further increase the switching energy barrier.^{10, 31} However, reducing the coercive field becomes challenging in ultra-thin film systems due to their small crystallite size as a result of interface effects.^{15, 32-36} To reduce the device dimensions without compromising ferroelectric performance, optimizing the film growth conditions for strain relaxation becomes crucial to achieve high quality AlScN films at sub-20nm thickness.

In the past several years, various metal films, including {111}-textured Pt and Al, were reported as effective AlScN growth templates to achieve ferroelectric capacitors (FeCaps) and ferroelectric field-effect transistors (FE-FETs).^{17, 37-40} However, the strain induced by lattice mismatch in the AlScN unit cell causes a high ferroelectric switching energy barrier in ultra-thin films, resulting in consistently high energy consumption for data storage.^{19, 31} Compared to Al (111), which has an in-plane lattice parameter of 2.86 Å, scandium (Sc) has a hexagonal crystal structure (like AlN) with an *a*-lattice parameter equal to 3.29 Å.^{41, 42} This leads to a lower lattice mismatch with AlScN, which has an *a*-lattice parameter that ranges from 3.11 Å to 3.53 Å depending upon the concentration of Sc (0% to 50.8%).^{43, 44} We posit that the utilization of this closer-matched templating layer could facilitate ultra-thin film polarization switching at lower applied electric fields by aiding in the reduction of interfacial strain. We explore this hypothesis explicitly in this report.

RESULTS AND DISCUSSION

To verify and evaluate the ferroelectric performance of the AlScN films grown on different templates, we fabricated bottom electrode/ $\text{Al}_{0.64}\text{Sc}_{0.32}\text{N}/\text{Al}$ FeCaps where the metal bottom electrode was either Al or Sc. The device cross-section structure depiction is shown in Figure 1a. The material exhibits Nitrogen-Polarity (N-polar) after deposition and becomes Metal-Polar (M-polar) by applying an electric field larger than the coercive field. The low magnification transmission electron microscopy (TEM) image in Figure 1d shows the thickness of each layer from Sc/ $\text{Al}_{0.68}\text{Sc}_{0.32}\text{N}/\text{Al}$. The thickness of Al/ $\text{Al}_{0.68}\text{Sc}_{0.32}\text{N}/\text{Al}$ obtained from TEM shown in Figure S3a. X-ray reflectometry (XRR) spectra (Figure S1) were employed to confirm the thickness of $\text{Al}_{0.68}\text{Sc}_{0.32}\text{N}$ grown on the two growth templates. In this work we chose the thicknesses obtained from the TEM when calculating the E_C of the FeCaps. This resulted in a slightly higher thickness for the AlScN fabricated on the Al template. This choice leads to the lowest E_C value for the Al/AlScN/Al FeCaps, and a slightly lower thickness for the AlScN fabricated on the Sc template, which leads to the highest E_C value for the Sc/AlScN/Al caps. This selection results in the most conservative analysis when comparing E_C reduction resulting from the better lattice matched Sc template. In Figure 1c, an X-Ray Diffraction (XRD) θ - 2θ scan from 30° to 40° shows that $\text{Al}_{0.32}\text{Sc}_{0.68}\text{N}$ and Sc have a strong c -axis out-of-plane orientation. A rocking curve (RC) ω -scan on the Sc 002 reflection generated a Full-Width-Half-Maximum (FWHM) of $\sim 0.76^\circ$, indicating the growth of a highly textured Sc film (Figure S2a). In the AlScN deposited on Al, a 002 peak is observed due to the film's low thickness and allows for the c lattice parameter to be extracted. For the AlScN film deposited on the GaN/Sc template, strong diffuse scattering from the GaN makes it challenging to accurately fit the AlScN 002 peak (Figure S2b). The a -lattice parameters of Sc and Al were measured by XRD. Based on the 002 and 101 reflections for

Sc, the a lattice parameter was calculated to be 3.308 Å. From the 111 and 200 reflections of Al, an a lattice parameter of 4.050 Å was determined, corresponding to an equivalent hexagonal close-packed (hcp) a lattice parameter of approximately 2.86 Å. Furthermore, Selected Area Electron Diffraction (SAED) along the AlScN $[11\bar{2}0]$ and Al $[1\bar{1}0]$ zone-axis, as shown in Figure 1e and Figure S3b, demonstrate the d -spacing difference of each thin film layer. Energy Dispersive X-ray Spectroscopy (EDS) mapping tracks the elemental composition of the two film stacks (Figure S4 and Figure S5), showing uniform distribution of various elements in their respective layers. Gallium at the bottom electrode/AlScN interface was introduced by ion beam damage during sample preparation. Oxygen was detected on the top Al electrode and Sc layer because of oxidation of the TEM sample when exposed to air. High-magnification TEM images show the interfaces between the ultra-thin $\text{Al}_{0.68}\text{Sc}_{0.32}\text{N}$ film and two types of bottom electrodes (Figure 1f and Figure S3c).

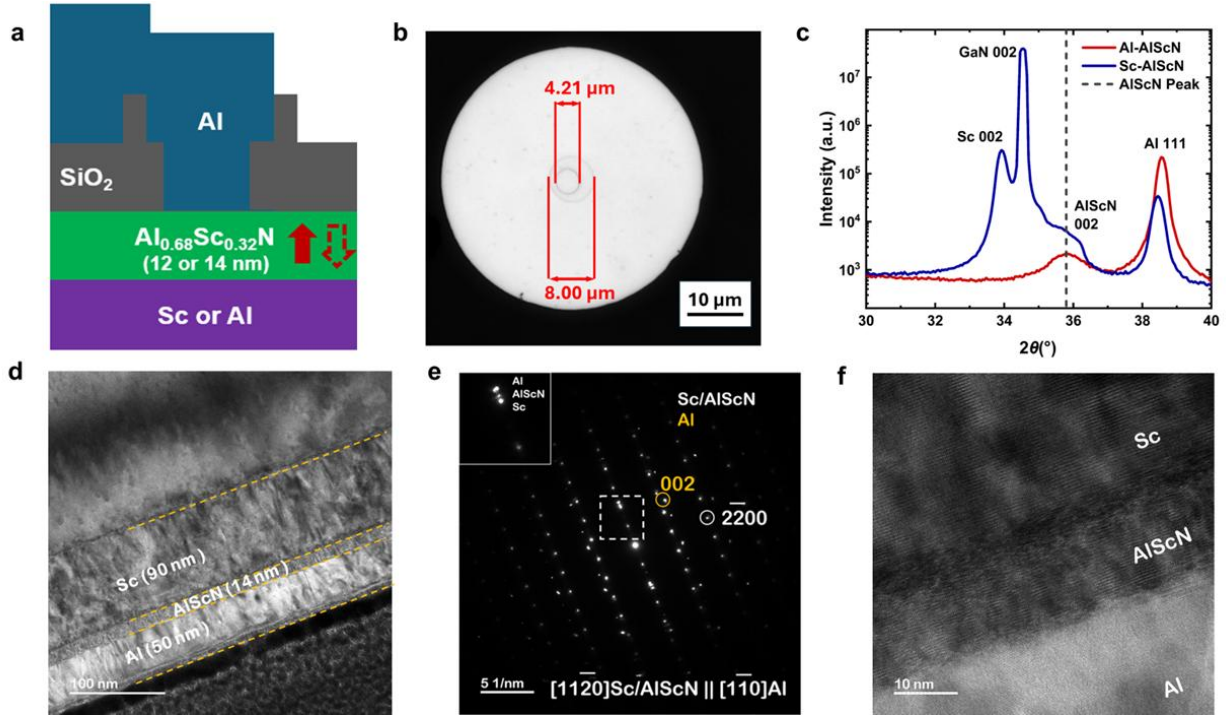


Figure 1. Device layout and material structure. (a) Cross-section schematic of $\text{Al}_{0.68}\text{Sc}_{0.32}\text{N}$ ferroelectric capacitors constructed with different bottom electrodes. The dashed arrow in the $\text{Al}_{0.68}\text{Sc}_{0.32}\text{N}$ layer represents the ferroelectric dipole direction after deposition while the solid red arrow represents the direction of the dipole after switching. (b) Optical Microscopy (OM) images of a single FeCap with $\sim 4 \mu\text{m}$ radius top electrode and $\sim 2.1 \mu\text{m}$ radius via. (c). $\theta/2\theta$ scan from 30° to 40° of GaN/Sc/AlScN/Al and Al/AlScN/Al films, showing Sc 002, GaN 002, AlScN 002 and Al 111 peaks. The AlScN peak labeled with a dash line is a peak fitting result of the AlScN 002 for the Al/AlScN/Al device. (d) Cross-sectional low-magnification TEM image showing 90 nm Sc, 14 nm AlScN and 50 nm Al FeCap layers. The interfaces between various layers have been marked by yellow dotted lines. (e) SAED pattern from the Sc/AlScN/Al region along $[11\bar{2}0]$ of Sc/AlScN and $[\bar{1}10]$ of Al. Insert is a magnified section (white dashed boxed region) presenting the out-of-plane spots, showing the different spacings for the three layers (f) High-magnification image of AlScN and the interfaces between Sc/AlScN and AlScN/Al.

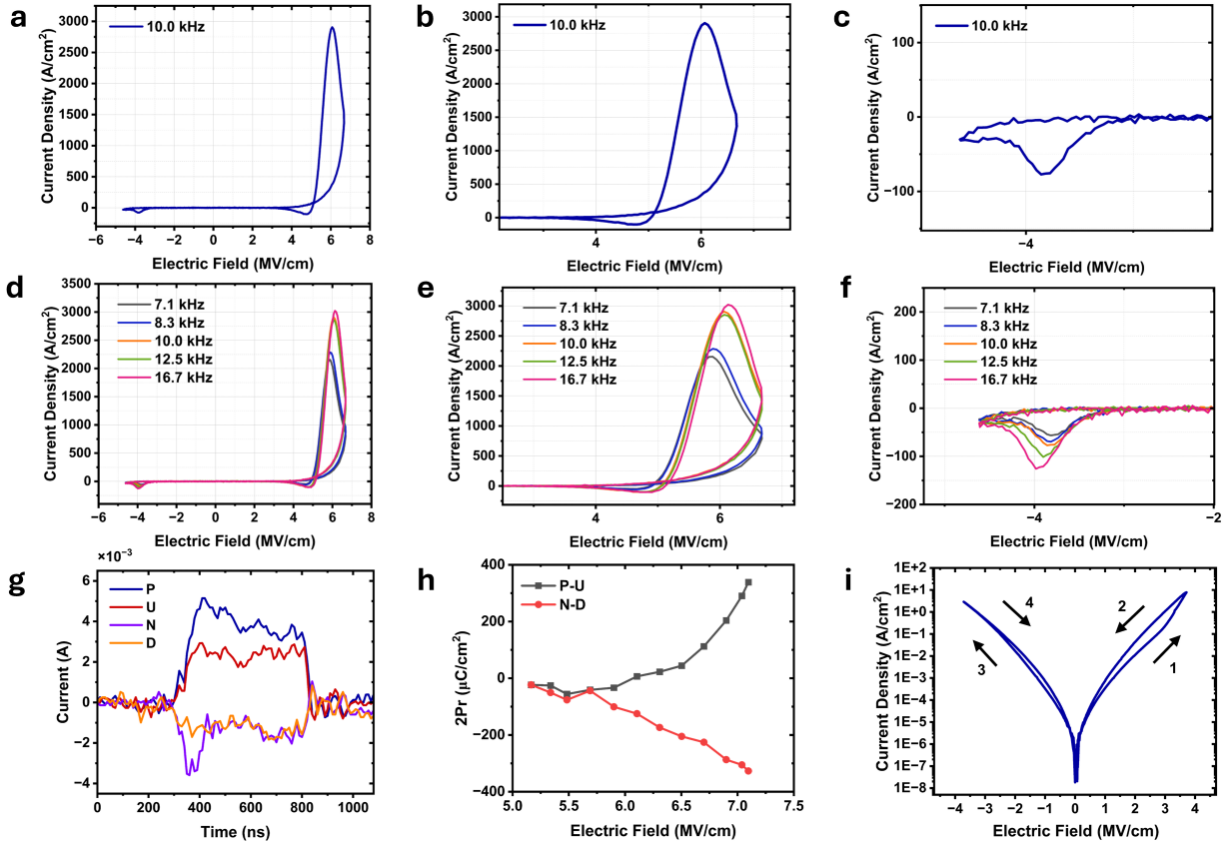


Figure 2. Ferroelectric performance of Sc/Al_{0.68}Sc_{0.32}N/Al capacitors. (a) Triangular PUND J-E hysteresis loop under 10 kHz triangular pulses. (b) Magnified image of positive electric-field-induced switching behavior under 10 kHz. (c) Magnified image of negative electric-field-induced switching behavior at 10 kHz. (d) Triangular PUND J-E hysteresis loops under different frequencies. (e) Magnified image of positive electric-field-induced switching performance at different frequencies. (f) Negative electric-field-induced switching comparison at different frequencies. (g) Current-Time response of rectangular PUND measurement with applied electric field of 7.23 MV/cm overlaid in time. The voltage is applied at 9.95 μ s with a rise/fall time of 20 ns. (h) Polarization change with applied electric field obtained from rectangular PUND measurement. (i) Counterclockwise (CCW) quasi-DC I-V sweep following a sweeping path from 1 to 4.

To study and evaluate the ferroelectric performance of Sc/Al_{0.68}Sc_{0.32}N/Al capacitors, electrical measurements were conducted using a Keithley 4200A-SCS analyzer. AC J-E hysteresis loops, Positive-Up-Negative-Down (PUND) tests, and DC I-V sweeps were used to analyze the switching behavior of the films. A 4.5 kHz triangular waveform (Figure S6(a)) was applied to the device over a specified electric field range from 6.7 MV/cm to -4.6 MV/cm. In Figure S6(b), both positive coercive field (E_C^+) and negative coercive field (E_C^-) can be clearly observed and are determined

to be 5.93 MV/cm and -4.02 MV/cm, respectively. The asymmetry in the coercive field between positive and negative sweeps is driven by the imprint effect, which has been frequently observed in sputtered AlScN films.^{45, 46} The switching and leakage behaviors were investigated by varying sweeping frequencies, as illustrated in Figure S7. Ferroelectric switching requires higher electric fields at higher frequencies due to the reduced dipole reorientation time and pinning effects, hindering domain motion and increasing the switching barrier.⁴⁷⁻⁵¹ As the frequency increases, the negative coercive fields become more pronounced (Figure S7(c)), whereas the ferroelectric switching at positive electric fields gradually merges with the resistive leakage peak (Figure S7(b)), making its precise identification more challenging.

To clearly observe the E_C , a triangular PUND technique previously applied to identify the ferroelectricity in AlScN thin film FeCaps under elevated temperatures was employed (Figure S8(a)).⁵² Two sets of triangular I-V pulses were utilized. The response to the first pulse shows both ferroelectric switching and leakage currents, while the response to the second pulse measured only leakage. The compensated current density peak was obtained by subtracting the first peak from the second (Figure S8(b)). In Figure 2a-2c, a triangular PUND test of the capacitor at 10 kHz excitation is presented. It shows pronounced ferroelectric switching peaks. The E_C^+ and E_C^- could be clearly identified after leakage subtraction as 6.06 MV/cm and -3.86 MV/cm, respectively. This technique was further applied across frequencies. In Figure 2d, a sweep range from 6.7 MV/cm to -4.6 MV/cm was maintained to ensure consistency with the single J-E hysteresis loop setup. Notably, switching events became more clearly defined after leakage subtraction for both positive and negative applied fields.

To further detect the dipole switching while gradually increasing the applied electric field, rectangular PUND measurements with 500 ns pulses were conducted. Reducing the pulse duration

reduces the impact from resistive leakage for ultra-thin film AlScN materials,^{19, 53} enabling more accurate measurement of the switching polarization ($2P_r$). The $2P_r$ is found by subtracting the polarization measured during the “U” and “D” pulses from that measured during the “P” and “N” pulses. Using 500 ns rectangular pulses (Figure S9(a)), clear dipole switching could be observed via current time response under an applied voltage of 10.13 V, as shown in Figure S9 (b), and after time overlaying the responses to each pulse as shown in Figure 2g. The switching from N-polar to M-polar using positive applied electric fields exhibited a slower switching response than when switching from M-polar to N-polar using negative applied electric fields. As shown in Figure 2h, polarization switching was first observed at ~ 5.7 MV/cm. The polarization increased with applied electric fields, reflecting the progressive switching process. However, precise determination of the saturated polarization remained challenging due to the high leakage observed in the ultra-thin film.⁵⁴⁻⁵⁶

Next, quasi-DC I-V measurements were conducted to investigate switching performance under slow sweeping conditions. A DC I-V hysteresis measurement was performed on the capacitor, sweeping from 5.2 V to -5.2 V with a 0.025 V step size. In Figure 2i, counterclockwise (CCW) current density sweeping behavior was observed, with higher current density along paths 2 and 4. To examine the electric-field-induced dipole switching, the first derivative of current with respect to voltage vs. the applied field was plotted (Figure S10). The peaks in the $\frac{di}{dV}$ response at 3.30 MV/cm and -3.28 MV/cm correspond to the ferroelectric dipole switching, which caused an abrupt increase in current. The measurement exhibited asymmetric sweeping consistent with the previously reported ferrodiode effect in AlScN.^{1, 57}

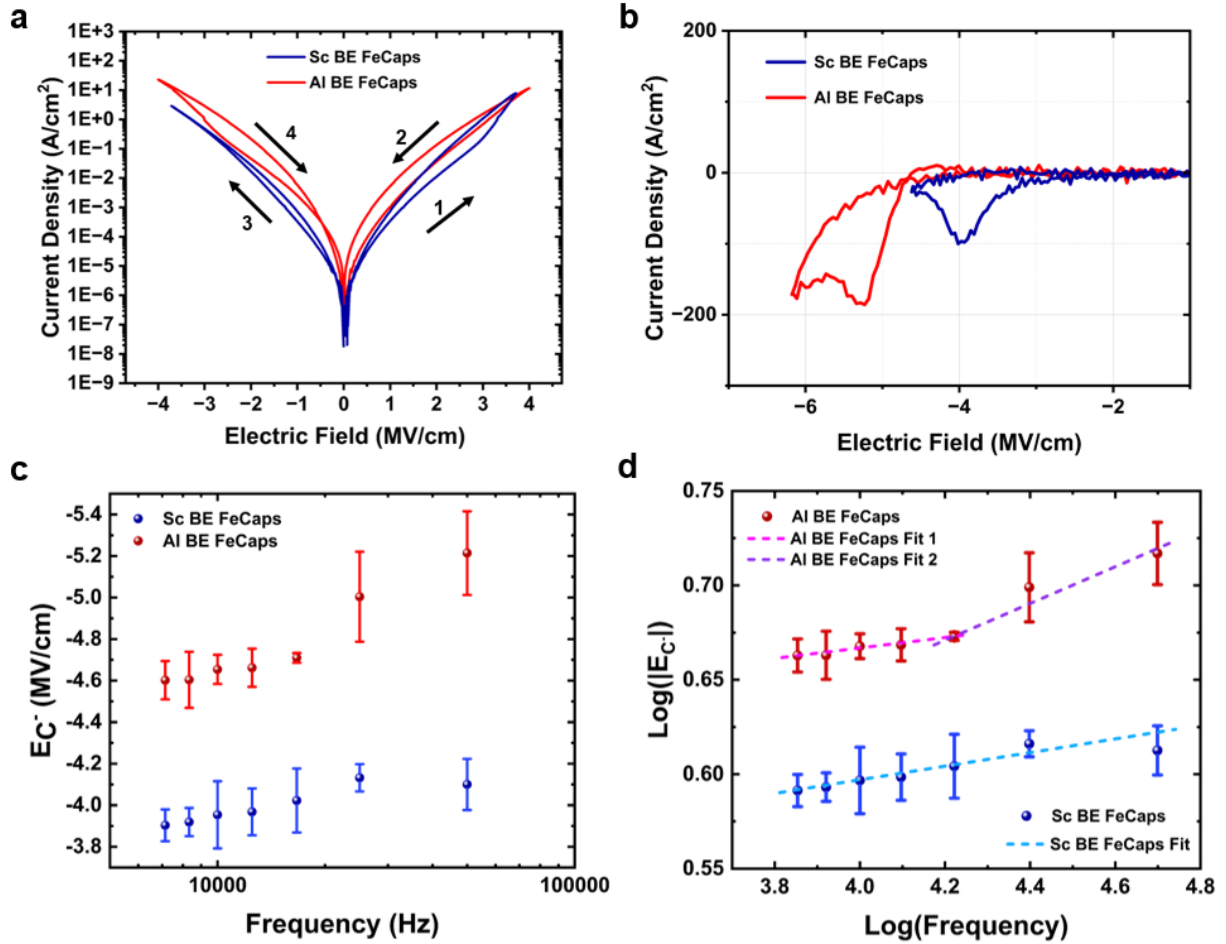


Figure 3. Ferroelectricity comparison of AlScN on Sc and Al bottom electrodes. (a) Quasi-DC I-V sweeping current density vs. applied electric field. (b) E_C^- comparison between Sc/Al_{0.68}Sc_{0.32}N/Al capacitors and Al/Al_{0.68}Sc_{0.32}N/Al capacitors via 25 kHz Triangular PUND J-E hysteresis loops. (c) E_C^- with error bars versus frequency for the capacitors with different bottom electrodes. (d) Logarithmic power-law fitting of $|E_C^-|$ vs. frequency for Sc BE FeCaps and Al BE FeCaps over a frequency range from 7.1 kHz to 50 kHz.

The ferroelectric behavior of Al_{0.68}Sc_{0.32}N grown on Sc and Al bottom electrodes is compared by focusing on their switching performance and frequency dependence using DC and AC electrical measurement conditions, as shown in Figure 3. In Figure 3a, the CCW DC I-V sweep of both devices – which tracks the change in current density with the applied electric field – shows that FeCaps based on AlScN with an Al electrode exhibit higher leakage current before the onset of

polarization switching. The E_C for positive and negative switching has been determined by the 1st derivative of the current with respect to voltage, $\frac{di}{dV}$, versus electric field (Figure S11). The measured E_C for positive and negative switching on FeCaps grown on an Al bottom electrode (Al BE) are 3.92 MV/cm and -3.67 MV/cm, respectively. Compared with Al BE FeCaps, those with Sc bottom electrode (Sc BE) show reduced E_C by 15.8% (E_C^+) and 10.6% (E_C^-).

Figure 3b shows the switching performance under AC I-V conditions. A triangular PUND pulse test at 25 kHz was conducted on Sc BE FeCaps and Al BE FeCaps, indicating an E_C^- of -4.02 MV/cm and -5.23 MV/cm, respectively. This corresponds to a ~23.1% reduction in E_C^- for the FeCaps grown on Sc. FeCaps grown on an Al BE exhibit more substantial resistive leakage at negative applied electric field, consistent with the behavior observed in the DC I-V sweeps. The higher applied electric field (8.80 MV/cm to -6.17 MV/cm) in FeCaps on Al electrodes, compared to the lower field range (6.40 MV/cm to -4.62 MV/cm) in FeCaps on Sc electrodes, facilitates lower leakage and direct observation of FE switching from N-polar to M-polar at positive electric fields on the Sc electrodes as shown in Figure 3b. Due to the high leakage observed for FeCaps made from ultra-thin AlScN films,¹⁹ the ferroelectric switching and resistive leakage peaks overlap at all frequencies, making a direct comparison of the E_C^+ between the two devices using AC I-V challenging (Figure S12 a and b). The J-E hysteresis loop without leakage subtraction (Figure S13), however, shows the Sc BE FeCaps have lower E_C^+ .

To better understand the switching dynamics and improve the reliability of our analysis, we measured E_C^- values vs. frequency on five randomly selected capacitors with a 4 μm radius. The mean E_C^- and standard deviation (SD) were calculated, from which symmetric error bars were generated. In Figure 3c, Sc BE FeCaps exhibit lower E_C^- . Notably, the E_C^- reduction becomes

larger at higher frequencies, with a 21.4% reduction observed at 50 kHz. The Kolmogorov–Avrami–Ishibashi (KAI) theory, which has been widely used to describe the switching-frequency dependence of ferroelectrics (Equation 1),^{58, 59} was used to describe the dynamic switching response of this ultra-thin AlScN film system. A linear relationship between $\log(|E_C^-|)$ and $\log(f)$ was obtained via logarithmic transformation of Equation 1 into Equation 2. Equation 2 was used to fit the experimental E_C^- - frequency data where E_0 is the coercive field under DC excitation, f is the experimental frequency, and α is the exponent that characterizes the dependence of E_C^- on frequency. E_C^- is the experimental kinetic negative coercive fields while E_0^- is the negative coercive field under DC excitation obtained from the fitting.

$$E_C = E_0 \cdot f^\alpha \quad (1)$$

$$\log(|E_C^-|) = \alpha \cdot \log(|E_C^-|) + \log(|E_0^-|) \quad (2)$$

The logarithmic fitting in Figure 3d shows that, at frequencies below 16.7 kHz, the E_C^- vs. frequency relationship of the Sc BE FeCaps and Al BE FeCaps follows $E_C \propto f^{0.036}$ and $E_C \propto f^{0.028}$ respectively (Table S1), suggesting reduced frequency dependence of the coercive field when comparing to a previous study reporting measurements of thicker AlScN film grown by Pulsed Laser Deposition (PLD).⁶⁰ The $|E_0|$ obtained from the fitting are 2.84 MV/cm and 3.60 MV/cm as reported in Table S1.

Interestingly, the Al BE FeCaps follow $E_C \propto f^{0.097}$ at higher frequencies, indicating a stronger frequency dependence of ferroelectric switching for faster external pulses. Chen *et al.* reported a similar phenomenon in a relaxor-based ferroelectric material, where the switching dynamics were separated into two frequency regimes due to domain kinetics differences at low and high

frequencies.⁶¹ It suggests that the observed behavior in Al BE FeCaps may also be linked to domain kinetics, although further investigation is required to validate this hypothesis.

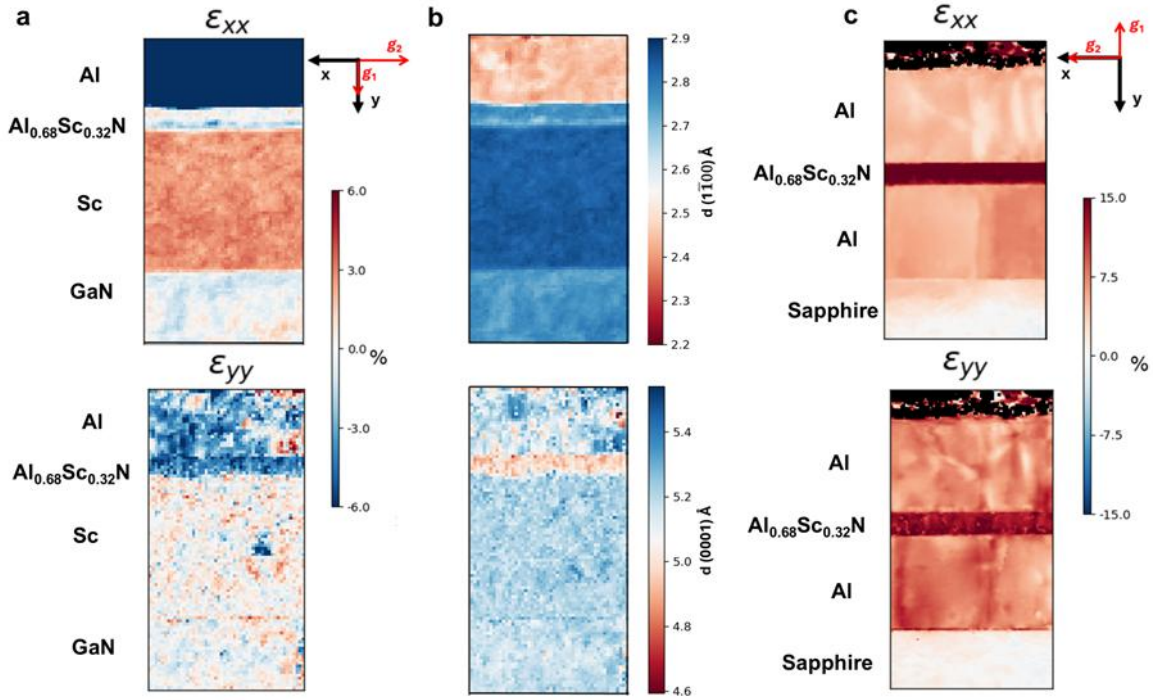


Figure 4. Scanning Electron Nanobeam Diffraction strain mapping of (a) ϵ_{xx} and ϵ_{yy} of GaN/Sc/Al_{0.68}Sc_{0.32}N/Al with respect to GaN, along $[1\bar{1}00]$ of GaN. (b) d -spacing map of GaN/Sc/Al_{0.68}Sc_{0.32}N/Al stack along in-plane $[1\bar{1}00]$ and out-of-plane $[0002]$ of AlScN, respectively. (c) ϵ_{xx} and ϵ_{yy} of sapphire/Al/Al_{0.68}Sc_{0.32}N/Al with respect to sapphire, along $[1\bar{1}00]$ of sapphire.

To investigate the effect of the bottom electrode on the structural strain, Scanning Electron Nanobeam Diffraction (SEND) was performed on the entire layer stack of each capacitor.⁶² Variations of the reciprocal lattice vector \vec{g} ($|\vec{g}| = 1/d_{spacing}$, where $d_{spacing}$ is the interplanar distance) were measured and then converted to a real space strain tensor,⁶³ following the

mathematical relationship in Equation 3. ε_{xx} and ε_{yy} correspond to the in-plane (horizontal) strain tensor and out-of-plane (vertical) strain tensor, calculated using Equation 4 and Equation 5, where d_{ref} is the reference $d_{spacing}$. In this work, the $d_{spacing}$ of GaN and sapphire were selected as the reference d_{ref} . These were calculated from the standard lattice parameters from the Joint Committee on Powder Diffraction Files (JCPDF). JCPDF number: 500792 for GaN $a=2.76 \text{ \AA}$, $c=5.18 \text{ \AA}$; JCPDF number: 740323 for sapphire $a=2.38 \text{ \AA}$, $c=4.33 \text{ \AA}$. d_{film} is the strained film interplanar spacing.

$$\varepsilon = \frac{d_{film} - d_{ref}}{d_{ref}} = \frac{\Delta d}{d_{ref}} \quad (3)$$

$$\varepsilon_{xx} = \frac{\Delta d_x}{d_{ref_{xx}}} \quad (4)$$

$$\varepsilon_{yy} = \frac{\Delta d_y}{d_{ref_{yy}}} \quad (5)$$

The strain map for the thin films was measured along the along $[\bar{1}100]$ and along $[0002]$ crystallographic directions of AlScN relative to the underlying substrate, shown in Figure 4. For the Sc and Al bottom electrodes, the substrates were GaN and sapphire, respectively. The results show that both electrodes are strained relative to their substrates, and this strain is transferred to the overlaying AlScN thin films. Notably, in Figure 4a, the AlScN film grown over the Sc bottom electrode exhibits in-plane strain (ε_{xx} mapping) comparable to GaN due to their similar in-plane lattice parameters. The strain tensor near the interface (bluish region) in the ε_{xx} map is attributed to the non-uniform interface formed between the Sc bottom electrode and the AlScN film. The ε_{yy} map shows that AlScN has smaller out-of-plane strain values across the film

relative to GaN, which is consistent with the smaller lattice parameter along the [0002] direction. The dark blue at the top Al layer in ϵ_{xx} is due to the cubic symmetry of Al contrasting with the hexagonal closed packed (hcp) structure of the underlying layers, as well as the chosen strain color scale being optimized to better highlight variations in the Sc and AlScN layers. Corresponding lattice parameter maps, shown in Figure 4b, further confirm the in-plane lattice match between GaN and AlScN, resulting in relatively lower strain between the Sc and AlScN at their interface. In contrast, the Al bottom electrode film exhibits a significant lattice mismatch compared to sapphire (Figure S14), leading to higher ϵ_{xx} and ϵ_{yy} values, as shown in Figure 4c. This larger strain induces greater strain variation across the AlScN grown on the Al bottom electrode in comparison to the more uniform strain distribution observed for the thin film with a Sc bottom electrode. Averaged lattice parameters for each layer of the film stacks were also determined from the SAED patterns and XRD and are summarized in Table 1, XRD values are rounded to match the resolution of the TEM measurements.

Table I. Experimentally Measured Lattice Constants Using TEM SAED patterns and XRD

Layers		GaN/Sc/AlScN/Al		Sapphire/Al/AlScN/Al	
		TEM	XRD	TEM	XRD
Sc	a (Å)	3.30	3.31		
	c (Å)	5.28	5.28		
AlScN	a (Å)	3.19	-	3.16	-
	c (Å)	5.02	5.04	5.01	5.01
Al	a (Å)	4.03	4.05	4.03	4.04

* XRD values are rounded from four to two decimal places for consistency with TEM measurements.

For the strain mapping, the underlying GaN and sapphire—being substantially thicker than the thin film stacks—were selected as strain-free references. Although the choice of reference affects the absolute strain quantification due to the d_{spacing} variations and does not allow a direct distinction between tensile and compressive strain, a clear contrast in the overall residual strain level can still be observed. Specifically, the ultra-thin AlScN film grown on the Sc bottom electrode, which has a smaller lattice mismatch with AlScN, exhibits lower in-plane residual strain compared to the film grown on the Al electrode.

Interestingly, both single-pattern diffraction analysis and strain mapping of the entire layer structure suggest that the in-plane and out-of-plane lattice parameters of ultra-thin $\text{Al}_{0.68}\text{Sc}_{0.32}\text{N}$ vary slightly between the two samples, resulting in a small difference in the c/a ratio, which is a key knob to tune the ferroelectricity in AlScN. In the case of AlScN on Sc the c/a ratio is ~ 1.57 , while it is ~ 1.58 for the ultra-thin film grown on Al. Despite this minimal difference in c/a , the Sc-based film displays a significantly lower coercive field and a different frequency dependence of E_C . Several factors may contribute to this observation. First, reduced interfacial strain may promote improved c -axis texture in the AlScN thin film. McMitchell *et al.* reported that modifying strain using different lattice-mismatched growth templates can influence the c -axis orientation in ultra-thin AlScN films, thereby affecting both the E_C and the Sc incorporation window in AlN.⁶⁴ The XRD measurements, however, do not show a significant difference in the c -axis orientation between the two AlScN films. Second, misfit dislocations generated by lattice mismatch and strain in the film may interact with domain walls, leading to a pinning effect that hinders 180° domain wall motion in wurtzite ferroelectric systems, thus suppressing switching behavior.⁶⁵⁻⁶⁸ The stronger frequency dependence of the E_C at higher frequencies supports higher domain wall pinning in the AlScN films grown on the Al electrode with higher lattice mismatch. The effect of

dislocations in PZT films has been widely studied,⁶⁹ while this topic is less explored in the AlScN system. To further elucidate the role of dislocations in AlScN, future studies using atomically resolved high-angle annular dark field (HAADF) and annular bright field (ABF) STEM imaging could help identify dislocations with different Burgers vectors near the interface.^{70, 71} These potential approaches underscore the importance of defect engineering in the development of scaled AlScN ferroelectric memory device.

CONCLUSION:

Ultra-thin AlScN films were deposited on Sc and Al bottom electrodes with clear *c*-axis orientation based on XRD and electron diffraction patterns. The ferroelectricity of AlScN grown on a Sc bottom electrode was extensively verified and evaluated, showing robust ferroelectricity both under AC and quasi-DC sweeps. By comparing the ferroelectric performance to capacitors with an Al bottom electrode, the Sc BE FeCaps demonstrated E_C reduction 15.8% (E_{C+}) and 10.6% (E_{C-}) under quasi-DC measurements. Furthermore, under AC conditions, the reduction of E_C depends on the frequency. At 50 kHz, the E_{C-} reduction can be more than 20%, indicating lower switching energy barrier realized by smaller-lattice mismatched Sc growth templates.

Applying the KAI model, the dynamic switching behavior of the two capacitors was evaluated. The ferroelectric ultra-thin film grown on Sc maintains a stable frequency dependency of coercive field across a wide frequency range (7.1 kHz to 50 kHz), while the AlScN film grown on Al has a higher frequency dependency for the coercive field at higher frequencies. To understand the mechanism behind the E_C reduction, strain mappings and the in-plane and out-of-plane lattice parameters for the film stacks were measured via SEND for the two samples. These measurements show that the ultra-thin $\text{Al}_{0.68}\text{Sc}_{0.32}\text{N}$ on Sc has lower in-plane strain, a larger *a*-axis lattice

parameter and a smaller lattice mismatch with the bottom electrode template. These results suggest that engineering the bottom electrode to minimize lattice mismatch at the interface is a promising strategy to tailor the ferroelectric properties of ultra-thin AlScN films, offering a viable route toward energy-efficient ferroelectric device design.

EXPERIMENTAL METHODS:

Film Deposition:

Scandium was selected as a novel growth template for AlScN ultra-thin films and was deposited onto a 5 μm GaN layer on a double side polished (DSP) 4-inch sapphire substrate via physical vapor deposition (PVD) using direct current (DC) sputtering. A 90 nm Sc film was deposited at 500 °C with a 20 standard cubic centimeters per minute (sccm) Ar gas flow under $\sim 1 \times 10^{-3}$ mbar and a target power of 1.27 W/cm². A 14 nm N-polar Al_{0.68}Sc_{0.32}N film was then synthesized in the same chamber without a vacuum break to prevent the oxidation of the bottom metal film. The AlScN ultra-thin film was deposited in a 30 sccm N₂ atmosphere (pressure range from 8~8.3 $\times 10^{-4}$ mbar) with an Al target power of 12.7 W/cm² and a Sc target power 8.32 W/cm² via reactive pulsed DC co-sputtering. This deposition was followed by the creation of a top Al electrode at 150 °C under a 20 sccm Ar atmosphere with a target power of 12.7 W/cm².

For comparing of the ferroelectric performance of ultra-thin Al_{0.68}Sc_{0.32}N films, a 50 nm Al bottom electrode was deposited on sapphire under the same conditions described above. An ~ 12 nm thick Al_{0.68}Sc_{0.32}N was subsequently synthesized followed by a 50 nm Al top electrode deposition. The entire film stack was deposited without breaking vacuum to prevent oxidation.

Device Fabrication

To fabricate the capacitors, photoresist on the Al top electrode was patterned with photolithography to construct 4 μm radius devices. This was followed by BCl_3/Cl_2 plasma etching, using an Oxford PlasmaPro 100 Cobra inductively coupled plasma (ICP) etcher, which also resulted in the exposure of bottom electrode. An ~ 90 nm thick layer of SiO_2 was selected as a dielectric material to create a larger probing pad, thereby avoiding direct contact of the probe with the thin ferroelectric capacitors. SiO_2 was deposited by chemical vapor deposition (CVD) at 200 $^\circ\text{C}$. Next, vias to each capacitor were constructed by photolithography and CF_4 plasma dry etching of the SiO_2 . An Ar plasma sputter etch was used to remove the alumina from the Al top electrode surface and was followed by in-situ ~ 100 nm Al deposition. The pad metal was then patterned by lithography and a BCl_3/Cl_2 plasma etching process. Device dimensions were acquired by Zeiss Axio Imager M2m Microscope.

Electrical Measurements:

Electrical measurements were conducted using a Keithley 4200A-SCS analyzer. For Alternative current (AC) measurement, triangular pulse J-E hysteresis loops with different frequencies were conducted on the FeCaps to verify the ferroelectricity. Triangular Positive-Up-Negative-Down (PUND) tests were performed on the devices with two types of bottom electrode to identify the E_C for comparison analysis. 500 ns ultra-fast rectangular PUND pulses were conducted on the Sc BE FeCaps to study the polarization switching. For DC I-V hysteresis analysis, a quasi-DC I-V (~ 0.01 Hz) voltage sweep with a 0.025 V step size was applied on the two FeCaps to analyze the E_C under quasi-DC conditions. All the tests were conducted with a 0.2-micron diameter, 2" long tungsten

flexible cat-whisker probe tip, for the top electrode and a standard 0.6 micro diameter tungsten probe tip for the bottom electrode.

Material Characterization:

For the cross-sectional TEM imaging of the thin films, a thin lamella suitable for the TEM analysis was prepared using a dual beam focused ion beam microscope (FEI Strata DB235). The lamella was thinned down to $\sim 1 \mu\text{m}$ using a Ga ion beam at 30 kV and 1 nA, followed by thinning down to $\sim 100 \text{ nm}$ at 30 kV and 100 pA current. To remove the damaged and amorphous surface layer, a low kV cleaning of the lamella was performed using 5kV and 30 pA ion beam. TEM imaging and scanning electron nanobeam diffraction (SEND) analysis were performed using a JEOL F200 microscope operating at 200 kV equipped with two image-forming cameras: OneView and low-dose electron counting Metro camera provided by GATAN. TEM images and SAED patterns were recorded using the OneView camera. A convergence angle of 2 mrad and 100 mm camera length were used to record the diffraction patterns (256 X 256) using the Metro camera. The data were further processed using py4DSTEM v. 0.14.18 provided by the National Center for Electron Microscopy, Lawrence Berkeley National Laboratory.⁷²

X-ray diffraction (XRD) and reflectivity (XRR) measurements were performed using a Panalytical X'Pert³ MRD diffractometer equipped with a Ge (220) double-bounce monochromator, a PIXcel detector, and a triple-axis point detector. Rocking curve measurements were conducted to determine the texture quality of the Sc film. Peak fitting of XRD reflections was used to extract lattice parameters, while XRR data were analyzed using GSAS-II, which employs the optical matrix method.⁷³

Corresponding Author

stach@seas.upenn.edu, rolsson@seas.upenn.edu

Author Contributions

Y.Z., R.R., E.S. and R.O. conceived the study. Y.Z. optimized film growth conditions, synthesized the metal-capacitor-metal film stacks, fabricated the devices, and measured the ferroelectric properties and R.O. supervised her. R.R performed the TEM characterization and strain mapping and E.S. supervised him. G.E. conducted XRD and XRR experiments. Y.W. assisted with fitting and methodology of electrical measurements under the supervision of D.J. Y.Z., R.R. and G.E. wrote the manuscript. All authors assisted with manuscript revisions. All authors have given approval to the final version of the manuscript.

Funding Sources

This work was partially supported by Intel Corporation under the SRS program. This work is supported in part by Army/ARL via the Collaborative for Hierarchical Agile and Responsive Materials (CHARM) under cooperative agreement W911NF-19-2-0119. This work was carried out in part at the Singh Center for Nanotechnology, which is supported by the NSF National Nanotechnology Coordinated Infrastructure Program under Grant NNCI-2025608. Additional support to the Nanoscale Characterization facility by the NSF through the University of Pennsylvania Materials Research Science and Engineering Center (MRSEC) (DMR-2309043) is acknowledged

REFERENCES

- (1) Kim, K.-H.; Han, Z.; Zhang, Y.; Musavigharavi, P.; Zheng, J.; Pradhan, D. K.; Stach, E. A.; Olsson III, R. H.; Jariwala, D. Multistate, ultrathin, back-end-of-line-compatible AlScN ferroelectric diodes. *ACS nano* **2024**, *18* (24), 15925-15934.
- (2) Pradhan, D. K.; Moore, D. C.; Kim, G.; He, Y.; Musavigharavi, P.; Kim, K.-H.; Sharma, N.; Han, Z.; Du, X.; Puli, V. S. A scalable ferroelectric non-volatile memory operating at 600° C. *Nature Electronics* **2024**, *7* (5), 348-355.
- (3) Fei, C.; Liu, X.; Zhu, B.; Li, D.; Yang, X.; Yang, Y.; Zhou, Q. AlN piezoelectric thin films for energy harvesting and acoustic devices. *Nano Energy* **2018**, *51*, 146-161.
- (4) Matloub, R.; Hadad, M.; Mazzalai, A.; Chidambaram, N.; Moulard, G.; Sandu, C.; Metzger, T.; Muralt, P. Piezoelectric Al_{1-x}Sc_xN thin films: A semiconductor compatible solution for mechanical energy harvesting and sensors. *Applied Physics Letters* **2013**, *102* (15).
- (5) Fichtner, S.; Wolff, N.; Lofink, F.; Kienle, L.; Wagner, B. AlScN: A III-V semiconductor based ferroelectric. *Journal of Applied Physics* **2019**, *125* (11).
- (6) Kim, K. D.; Ryoo, S. K.; Park, H. S.; Choi, S.; Park, T. W.; Yeom, M. K.; Hwang, C. S. Comparative study on the stability of ferroelectric polarization of HfZrO₂ and AlScN thin films over the depolarization effect. *Journal of Applied Physics* **2024**, *136* (2).
- (7) Yassine, M.; Nair, A.; Fammels, J.; Wade, E.; Fu, Z.; Yassine, A.; Kirste, L.; Ambacher, O. Influence of structural properties on the ferroelectric behavior of hexagonal AlScN. *Journal of Applied Physics* **2022**, *132* (11).
- (8) Mizutani, R.; Yasuoka, S.; Shiraishi, T.; Shimizu, T.; Uehara, M.; Yamada, H.; Akiyama, M.; Sakata, O.; Funakubo, H. Thickness scaling of (Al_{0.8}Sc_{0.2})N films with remanent polarization beyond 100 μC cm⁻² around 10 nm in thickness. *Applied Physics Express* **2021**, *14* (10), 105501.
- (9) Chen, L.; Liu, C.; Lee, H. K.; Varghese, B.; Ip, R. W. F.; Li, M.; Quek, Z. J.; Hong, Y.; Wang, W.; Song, W. Demonstration of 10 nm Ferroelectric Al_{0.7}Sc_{0.3}N-Based Capacitors for Enabling Selector-Free Memory Array. *Materials* **2024**, *17* (3), 627.
- (10) Qin, H.; He, N.; Han, C.; Zhang, M.; Wang, Y.; Hu, R.; Wu, J.; Shao, W.; Saadi, M.; Zhang, H. Perspectives of Ferroelectric Wurtzite AlScN: Material Characteristics, Preparation, and Applications in Advanced Memory Devices. *Nanomaterials* **2024**, *14* (11), 986.
- (11) Kim, K.-H.; Song, S.; Kim, B.; Musavigharavi, P.; Trainor, N.; Katti, K.; Chen, C.; Kumari, S.; Zheng, J.; Redwing, J. M. Tuning polarity in WSe₂/AlScN FeFETs via contact engineering. *ACS nano* **2024**, *18* (5), 4180-4188.
- (12) Liu, X.; Wang, D.; Kim, K.-H.; Katti, K.; Zheng, J.; Musavigharavi, P.; Miao, J.; Stach, E. A.; Olsson III, R. H.; Jariwala, D. Post-CMOS compatible aluminum scandium nitride/2D channel ferroelectric field-effect-transistor memory. *Nano Letters* **2021**, *21* (9), 3753-3761.
- (13) Wang, D.; Wang, P.; Mondal, S.; Liu, J.; Hu, M.; He, M.; Nam, S.; Peng, W.; Yang, S.; Wang, D.; et al. Controlled ferroelectric switching in ultrawide bandgap AlN/ScAlN multilayers. *Applied Physics Letters* **2023**, *123* (10).
- (14) Casamento, J.; Nomoto, K.; Nguyen, T.-S.; Lee, H.; Savant, C.; Li, L.; Hickman, A.; Maeda, T.; Shao, Y.-T.; Encomendero, J. AlScN high electron mobility transistors: Integrating high piezoelectric, high k dielectric, and ferroelectric functionality. In *2023 IEEE BiCMOS and Compound Semiconductor Integrated Circuits and Technology Symposium (BCICTS), 2023*; IEEE: pp 132-136.

- (15) Schönweger, G.; Wolff, N.; Islam, M. R.; Gremmel, M.; Petraru, A.; Kienle, L.; Kohlstedt, H.; Fichtner, S. In - grain ferroelectric switching in sub - 5 nm thin Al_{0.74}Sc_{0.26}N films at 1 V. *Advanced Science* **2023**, *10* (25), 2302296.
- (16) Wang, D.; Wang, P.; Mondal, S.; Hu, M.; Wang, D.; Wu, Y.; Ma, T.; Mi, Z. Thickness scaling down to 5 nm of ferroelectric ScAlN on CMOS compatible molybdenum grown by molecular beam epitaxy. *Applied Physics Letters* **2023**, *122* (5).
- (17) Kim, K.-H.; Oh, S.; Fiagbenu, M. M. A.; Zheng, J.; Musavigharavi, P.; Kumar, P.; Trainor, N.; Aljarb, A.; Wan, Y.; Kim, H. M. Scalable CMOS back-end-of-line-compatible AlScN/two-dimensional channel ferroelectric field-effect transistors. *Nature nanotechnology* **2023**, *18* (9), 1044-1050.
- (18) Wang, P.; Wang, D.; Mondal, S.; Hu, M.; Wu, Y.; Ma, T.; Mi, Z. Ferroelectric nitride heterostructures on CMOS compatible molybdenum for synaptic memristors. *ACS Applied Materials & Interfaces* **2023**, *15* (14), 18022-18031.
- (19) Zheng, J. X.; Fiagbenu, M. M. A.; Esteves, G.; Musavigharavi, P.; Gunda, A.; Jariwala, D.; Stach, E. A.; Olsson, R. H. Ferroelectric behavior of sputter deposited Al_{0.72}Sc_{0.28}N approaching 5 nm thickness. *Applied Physics Letters* **2023**, *122* (22).
- (20) Ryoo, S. K.; Kim, K. D.; Choi, W.; Sriboriboon, P.; Heo, S.; Seo, H.; Jang, Y. H.; Jeon, J. W.; Yeom, M. K.; Lee, S. H. Fabrication of Ultrathin Ferroelectric Al_{0.7}Sc_{0.3}N Films under Complementary - Metal - Oxide - Semiconductor Compatible Conditions by using HfN_{0.4} Electrode. *Advanced Materials* **2025**, *37* (1), 2413295.
- (21) Cho, H.; Lee, B.; Jang, D.; Yoon, J.; Chung, S.; Hong, Y. Recent progress in strain-engineered elastic platforms for stretchable thin-film devices. *Materials Horizons* **2022**, *9* (8), 2053-2075.
- (22) Shin, H.; Katiyar, A. K.; Hoang, A. T.; Yun, S. M.; Kim, B. J.; Lee, G.; Kim, Y.; Lee, J.; Kim, H.; Ahn, J.-H. Nonconventional strain engineering for uniform biaxial tensile strain in MoS₂ thin film transistors. *ACS nano* **2024**, *18* (5), 4414-4423.
- (23) Sun, F.; Chen, D.; Gao, X.; Liu, J.-M. Emergent strain engineering of multiferroic BiFeO₃ thin films. *Journal of Materiomics* **2021**, *7* (2), 281-294.
- (24) Kim, D. B.; Kim, J. Y.; Han, J.; Cho, Y. S. Strain engineering in power-generating and self-powered nanodevices. *Nano Energy* **2024**, 109551.
- (25) Kim, J. M.; Haque, M. F.; Hsieh, E. Y.; Nahid, S. M.; Zarin, I.; Jeong, K. Y.; So, J. P.; Park, H. G.; Nam, S. Strain engineering of low - dimensional materials for emerging quantum phenomena and functionalities. *Advanced Materials* **2023**, *35* (27), 2107362.
- (26) Jain, S.; Harker, A.; Cowley, R. Misfit strain and misfit dislocations in lattice mismatched epitaxial layers and other systems. *Philosophical Magazine A* **1997**, *75* (6), 1461-1515.
- (27) Hwang, D.-M. D. Strain relaxation in lattice-mismatched epitaxy. *Materials chemistry and physics* **1995**, *40* (4), 291-297.
- (28) Li, T.; Deng, S.; Liu, H.; Chen, J. Insights into strain engineering: from ferroelectrics to related functional materials and beyond. *Chemical Reviews* **2024**, *124* (11), 7045-7105.
- (29) Damodaran, A. R.; Agar, J. C.; Pandya, S.; Chen, Z.; Dedon, L.; Xu, R.; Apgar, B.; Saremi, S.; Martin, L. W. New modalities of strain-control of ferroelectric thin films. *Journal of Physics: Condensed Matter* **2016**, *28* (26), 263001.
- (30) Österlund, E.; Ross, G.; Caro, M. A.; Paulasto-Kröckel, M.; Hollmann, A.; Klaus, M.; Meixner, M.; Genzel, C.; Koppinen, P.; Pensala, T. Stability and residual stresses of sputtered wurtzite AlScN thin films. *Physical Review Materials* **2021**, *5* (3), 035001.

- (31) Musavigharavi, P.; Meng, A. C.; Wang, D.; Zheng, J.; Foucher, A. C.; Olsson III, R. H.; Stach, E. A. Nanoscale structural and chemical properties of ferroelectric aluminum scandium nitride thin films. *The Journal of Physical Chemistry C* **2021**, *125* (26), 14394-14400.
- (32) Li, X.; Fang, Y.; Zhou, J.; Li, B.; Wu, Z.; Fang, C.; Zeng, X.; Zheng, S.; Mao, W.; Hao, Y. Impact of Scaling Thickness on the Ferroelectric Properties of Pt/Al_{0.8}Sc_{0.2}N/Pt Capacitors. *IEEE Transactions on Electron Devices* **2025**, *72* (1), 370-375.
- (33) Chen, H.-Y.; Mo, C.-L.; Shyue, J.-J.; Huang, T.-Y.; Chen, M.-J. Probing Hf_{0.5}Zr_{0.5}O₂ Ferroelectricity: Neutron Reflectivity Reveals Critical Interface Effects. *ACS Applied Materials & Interfaces* **2025**, *17* (10), 16102-16110.
- (34) Han, M.-G.; Marshall, M. S.; Wu, L.; Schofield, M. A.; Aoki, T.; Twosten, R.; Hoffman, J.; Walker, F. J.; Ahn, C. H.; Zhu, Y. Interface-induced nonswitchable domains in ferroelectric thin films. *Nature communications* **2014**, *5* (1), 4693.
- (35) Wang, D.; Zheng, J.; Tang, Z.; D'Agati, M.; Gharavi, P. S.; Liu, X.; Jariwala, D.; Stach, E. A.; Olsson, R. H.; Roebisch, V. Ferroelectric c-axis textured aluminum scandium nitride thin films of 100 nm thickness. In *2020 joint conference of the ieee international frequency control symposium and international symposium on applications of ferroelectrics (IFCS-ISAF)*, 2020; IEEE: pp 1-4.
- (36) Zhang, Y.; Zhu, Q.; Tian, B.; Duan, C. New-generation ferroelectric AlScN materials. *Nano-Micro Letters* **2024**, *16* (1), 227.
- (37) Wang, D.; Musavigharavi, P.; Zheng, J.; Esteves, G.; Liu, X.; Fiagbenu, M. M. A.; Stach, E. A.; Jariwala, D.; Olsson III, R. H. Sub-Microsecond Polarization Switching in (Al,Sc)N Ferroelectric Capacitors Grown on Complementary Metal–Oxide–Semiconductor-Compatible Aluminum Electrodes. *physica status solidi (RRL) – Rapid Research Letters* **2021**, *15* (5), 2000575.
- (38) Song, S.; Kim, K.-H.; Keneipp, R.; Jung, M.; Trainor, N.; Chen, C.; Zheng, J.; Redwing, J. M.; Kang, J.; Drndic, M. High Current and Carrier Densities in 2D MoS₂/AlScN Field-Effect Transistors via Ferroelectric Gating and Ohmic Contacts. *ACS nano* **2025**, *19* (9), 8985-8996.
- (39) Song, S.; Kim, K.-H.; Chakravarthi, S.; Han, Z.; Kim, G.; Ma, K. Y.; Shin, H. S.; Olsson, R. H.; Jariwala, D. Negative capacitance field-effect transistors based on ferroelectric AlScN and 2D MoS₂. *Applied Physics Letters* **2023**, *123* (18).
- (40) Zhang, J.; Li, B.; Zhou, J.; Liu, Y.; Hao, Y.; Han, G. Leakage Study of Ferroelectric AlScN Capacitors Prepared on Different Bottom Electrodes. In *2024 9th International Conference on Integrated Circuits and Microsystems (ICICM)*, 2024; IEEE: pp 82-86.
- (41) Tang, F.; Che, X.; Lu, W.; Chen, G.; Xie, Y.; Yu, W. Surface structure and solidification morphology of aluminum nanoclusters. *Physica B: Condensed Matter* **2009**, *404* (16), 2489-2494.
- (42) Spedding, F. H.; Daane, A.; Herrmann, K. The crystal structures and lattice parameters of high-purity scandium, yttrium and the rare earth metals. *Acta Crystallographica* **1956**, *9* (7), 559-563.
- (43) Hirata, K.; Niitsu, K.; Anggraini, S. A.; Kageura, T.; Uehara, M.; Yamada, H.; Akiyama, M. Enhancing the piezoelectric performance of nitride thin films through interfacial engineering. *Materials Today* **2025**.
- (44) Deng, R.; Evans, S. R.; Gall, D. Bandgap in Al_{1-x}Sc_xN. *Applied Physics Letters* **2013**, *102* (11).
- (45) Gremmel, M.; Fichtner, S. The interplay between imprint, wake-up, and domains in ferroelectric Al_{0.7}Sc_{0.3}N. *Journal of Applied Physics* **2024**, *135* (20).

- (46) Schönweger, G.; Islam, M. R.; Wolff, N.; Petraru, A.; Kienle, L.; Kohlstedt, H.; Fichtner, S. Ultrathin Al_{1-x}Sc_xN for low-voltage-driven ferroelectric-based devices. *physica status solidi (RRL)–Rapid Research Letters* **2023**, *17* (1), 2200312.
- (47) Liu, F.; Fina, I.; Bertacco, R.; Fontcuberta, J. Unravelling and controlling hidden imprint fields in ferroelectric capacitors. *Scientific reports* **2016**, *6* (1), 25028.
- (48) Lee, C.-W.; Yazawa, K.; Zakutayev, A.; Brennecke, G. L.; Gorai, P. Switching it up: New mechanisms revealed in wurtzite-type ferroelectrics. *Science Advances* **2024**, *10* (20), ead10848.
- (49) Damjanovic, D. Logarithmic frequency dependence of the piezoelectric effect due to pinning of ferroelectric-ferroelastic domain walls. *Physical Review B* **1997**, *55* (2), R649.
- (50) Guido, R.; Lu, H.; Lomenzo, P. D.; Mikolajick, T.; Gruverman, A.; Schroeder, U. Kinetics of N-to-M-Polar Switching in Ferroelectric Al_{1-x}Sc_xN Capacitors. *Advanced Science* **2024**, *11* (16), 2308797.
- (51) Liu, S.; Grinberg, I.; Rappe, A. M. Intrinsic ferroelectric switching from first principles. *Nature* **2016**, *534* (7607), 360-363.
- (52) He, Y.; Moore, D. C.; Wang, Y.; Ware, S.; Ma, S.; Pradhan, D. K.; Hu, Z.; Du, X.; Kennedy, W. J.; Glavin, N. R.; et al. Al_{0.68}Sc_{0.32}N/SiC-Based Metal-Ferroelectric-Semiconductor Capacitors Operating up to 1000 °C. *Nano Letters* **2025**, *25* (12), 4767-4773.
- (53) Wang, D.; Zheng, J.; Musavigharavi, P.; Zhu, W.; Foucher, A. C.; Trolier-McKinstry, S. E.; Stach, E. A.; Olsson, R. H. Ferroelectric switching in sub-20 nm aluminum scandium nitride thin films. *IEEE Electron Device Letters* **2020**, *41* (12), 1774-1777.
- (54) Gao, Z.; Luo, Y.; Lyu, S.; Cheng, Y.; Zheng, Y.; Zhong, Q.; Zhang, W.; Lyu, H. Identification of ferroelectricity in a capacitor with ultra-thin (1.5-nm) Hf_{0.5}Zr_{0.5}O₂ film. *IEEE Electron Device Letters* **2021**, *42* (9), 1303-1306.
- (55) Chouprik, A.; Chernikova, A.; Markeev, A.; Mikheev, V.; Negrov, D.; Spiridonov, M.; Zarubin, S.; Zenkevich, A. Electron transport across ultrathin ferroelectric Hf_{0.5}Zr_{0.5}O₂ films on Si. *Microelectronic Engineering* **2017**, *178*, 250-253.
- (56) Chen, L.; Wang, Z.; Liu, C.; Li, M.; Song, W.; Wang, W.; Varghese, B.; Lee, H. K.; Lin, H.; Zhu, Y. Leakage mechanism of ferroelectric Al_{0.7}Sc_{0.3}N ultra-thin film. In *2023 IEEE International Symposium on Applications of Ferroelectrics (ISAF)*, 2023; IEEE: pp 1-3.
- (57) Liu, X.; Zheng, J.; Wang, D.; Musavigharavi, P.; Stach, E. A.; Olsson, R.; Jariwala, D. Aluminum scandium nitride-based metal-ferroelectric-metal diode memory devices with high on/off ratios. *Applied Physics Letters* **2021**, *118* (20).
- (58) Scott, J. Models for the frequency dependence of coercive field and the size dependence of remanent polarization in ferroelectric thin films. *Integrated Ferroelectrics* **1996**, *12* (2-4), 71-81.
- (59) Li, W.; Chen, Z.; Auciello, O. Calculation of frequency-dependent coercive field based on the investigation of intrinsic switching kinetics of strained Pb(Zr_{0.2}Ti_{0.8})O₃ thin films. *Journal of Physics D: Applied Physics* **2011**, *44* (10), 105404.
- (60) Liu, C.; Wang, Q.; Yang, W.; Cao, T.; Chen, L.; Li, M.; Liu, F.; Loke, D.; Kang, J.; Zhu, Y. Multiscale modeling of Al_{0.7}Sc_{0.3}N-based FeRAM: the steep switching, leakage and selector-free array. In *2021 IEEE International Electron Devices Meeting (IEDM)*, 2021; IEEE: pp 8.1.1-8.1.4.
- (61) Chen, Z.; Zhang, Y.; Li, S.; Lu, X.-M.; Cao, W. Frequency dependence of the coercive field of 0.71 Pb(Mg_{1/3}Nb_{2/3})O₃-0.29 PbTiO₃ single crystal from 0.01 Hz to 5 MHz. *Applied Physics Letters* **2017**, *110* (20).

- (62) Zuo, J.-M.; Tao, J. Scanning Electron Nanodiffraction and Diffraction Imaging. In *Scanning Transmission Electron Microscopy: Imaging and Analysis*, Pennycook, S. J., Nellist, P. D. Eds.; Springer New York, 2011; pp 393-427.
- (63) Hýtch MJ, M. A. Observing and measuring strain in nanostructures and devices with transmission electron microscopy. *MRS Bulletin* **2014**, *39* (2), 138-146.
- (64) McMitchell, S. R.; Walke, A. M.; Banerjee, K.; Mertens, S.; Piao, X.; Mao, M.; Katcko, K.; Vellianitis, G.; Van Dal, M.; Lin, Y.-M. Engineering strain and texture in ferroelectric scandium-doped aluminium nitride. *ACS Applied Electronic Materials* **2023**, *5* (2), 858-864.
- (65) Höfling, M.; Zhou, X.; Riemer, L. M.; Bruder, E.; Liu, B.; Zhou, L.; Groszewicz, P. B.; Zhuo, F.; Xu, B.-X.; Durst, K.; et al. Control of polarization in bulk ferroelectrics by mechanical dislocation imprint. *Science* **2021**, *372* (6545), 961-964.
- (66) Li, N.; Zhu, R.; Cheng, X.; Liu, H.-J.; Zhang, Z.; Huang, Y.-L.; Chu, Y.-H.; Chen, L.-Q.; Ikuhara, Y.; Gao, P. Dislocation-induced large local polarization inhomogeneity of ferroelectric materials. *Scripta Materialia* **2021**, *194*, 113624.
- (67) Lubk, A.; Rossell, M.; Seidel, J.; Chu, Y.; Ramesh, R.; Hýtch, M.; Snoeck, E. Electromechanical coupling among edge dislocations, domain walls, and nanodomains in BiFeO₃ revealed by unit-cell-wise strain and polarization maps. *Nano letters* **2013**, *13* (4), 1410-1415.
- (68) Dong, L.; Schnitker, J.; Smith, R. W.; Srolovitz, D. J. Stress relaxation and misfit dislocation nucleation in the growth of misfitting films: A molecular dynamics simulation study. *Journal of applied physics* **1998**, *83* (1), 217-227.
- (69) Gao, P.; Nelson, C.; Jokisaari, J.; Baek, S.; Bark, C.; Zhang, Y.; Wang, E.; Schlom, D.; Eom, C.; Pan, X. Revealing the role of defects in ferroelectric switching with atomic resolution. *Nat. Commun*: 2011.
- (70) Gao, P.; Ishikawa, R.; Feng, B.; Kumamoto, A.; Shibata, N.; Ikuhara, Y. Atomic-scale structure relaxation, chemistry and charge distribution of dislocation cores in SrTiO₃. *Ultramicroscopy* **2018**, *184*, 217-224.
- (71) Salamania, J.; Kwick, K. C.; Sangiovanni, D. G.; Tasnadi, F.; Abrikosov, I. A.; Rogström, L.; Johnson, L.; Odén, M. High-resolution STEM investigation of the role of dislocations during decomposition of Ti_{1-x}Al_xNy. *Scripta Materialia* **2023**, *229*, 115366.
- (72) Savitzky, B. H.; Zeltmann, S. E.; Hughes, L. A.; Brown, H. G.; Zhao, S.; Pelz, P. M.; Pekin, T. C.; Barnard, E. S.; Donohue, J.; Rangel DaCosta, L.; et al. py4DSTEM: A Software Package for Four-Dimensional Scanning Transmission Electron Microscopy Data Analysis. *Microscopy and Microanalysis* **2021**, *27* (4), 712-743. (accessed 5/21/2025).
- (73) Toby, B. H.; Von Dreele, R. B. GSAS-II: the genesis of a modern open-source all purpose crystallography software package. *Applied Crystallography* **2013**, *46* (2), 544-549.

(Supporting Information)

Coercive Field Reduction in Ultra-thin $\text{Al}_{1-x}\text{Sc}_x\text{N}$ via Interfacial Engineering with a Scandium Electrode

AUTHOR NAMES Yinuo Zhang,¹ Rajeev Kumar Rai,² Giovanni Esteves,³ Yubo Wang,¹ Deep
M. Jariwala,¹ Eric A. Stach^{2,*} and Roy H. Olsson, III^{1,*}

AUTHOR ADDRESS

1. Department of Electrical and Systems Engineering, University of Pennsylvania, Philadelphia, PA, USA 19104
2. Department of Materials Science and Engineering, University of Pennsylvania, Philadelphia, PA, USA 19104
3. Microsystems Engineering, Science and Applications (MESA) Center, Sandia National Laboratories, Albuquerque, NM, USA 87185

* Corresponding Authors: stach@seas.upenn.edu, rolsson@seas.upenn.edu

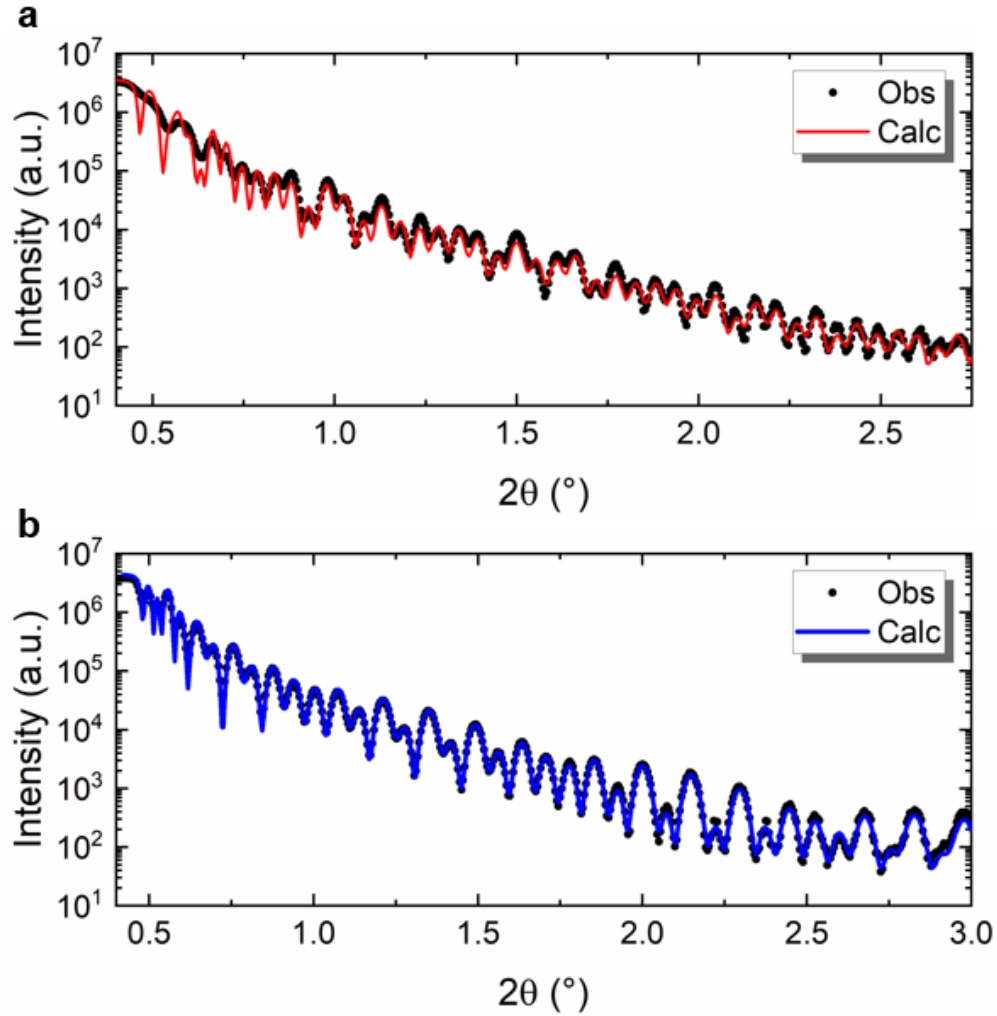


Figure S1. (a) XRR spectrum with fitting line (red) of AlScN on the Sc bottom electrode, obtaining a thickness 14.68 nm for AlScN (b) XRR spectrum with fitting line (blue) of AlScN on the Al bottom electrode, obtaining 10.77 nm thickness for the AlScN.

The fit for the Sc/AlScN electrode required modeling three distinct Al layers due to surface defects that caused increased roughness. Including these additional Al layers improved the fit of the XRR at angles below 1° . In contrast, the Al/AlScN sample did not exhibit such defects and was refined using the expected Al/AlScN/Al three-layer model. The error bars of ± 1 nm reflect variations from multiple least-squares refinement approaches applied to the XRR data.

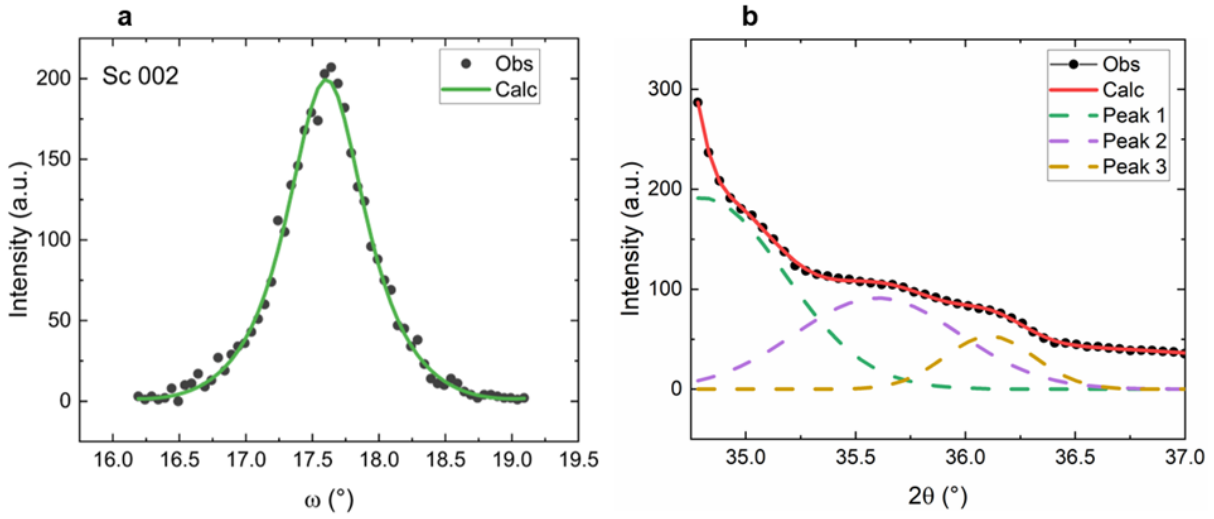


Figure S2. (a) Rocking curve scan of Sc 002, obtained a FWHM of 0.76° from peak fitting. (b) Distinguished peaks from convoluted 2θ scan of Sc/AlScN/Al. Peak 2 is used to calculate the c lattice parameter of the AlScN, even though on the θ - 2θ pattern in Figure 2 they appear to have similar peak positions. Strong diffuse scattering from the GaN, prevents peak fitting with a single peak that would otherwise solely represent the AlScN 002.

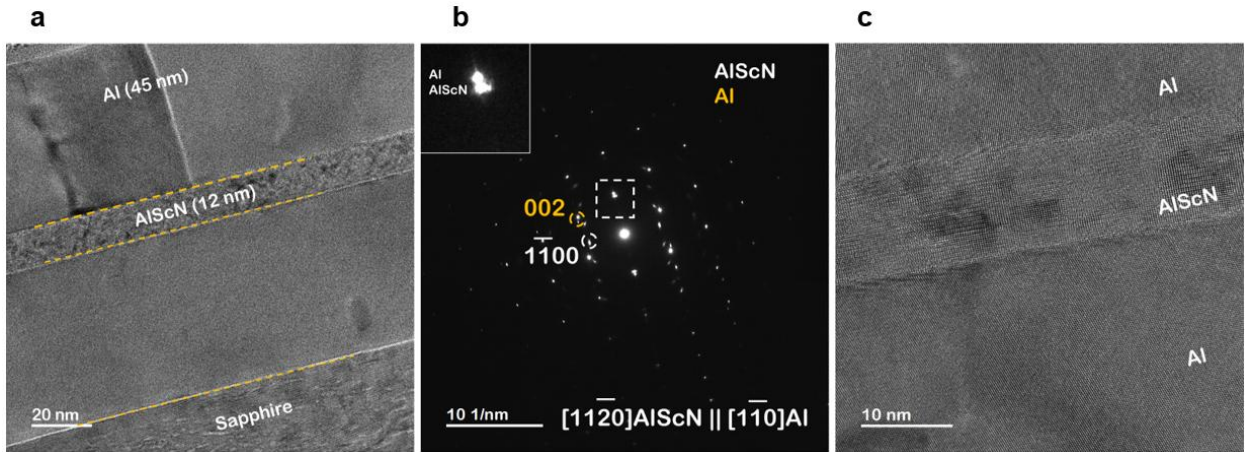


Figure S3. (a) Cross-sectional low-magnification TEM image showing the various thin film layers of sapphire/Al/AlScN/Al. The interfaces between various layer have been marked by yellow dotted lines (b) SAED pattern from the Al/AlScN/Al region along $[11\bar{2}0]$ of AlScN and $[1\bar{1}0]$ of Al, inset: zoomed in out-of-plane spots showing the 2 different lattice spacing corresponding to (0002) of AlScN and (111) of Al planes. (c) High-magnification image of AlScN and interfaces between Al & AlScN.

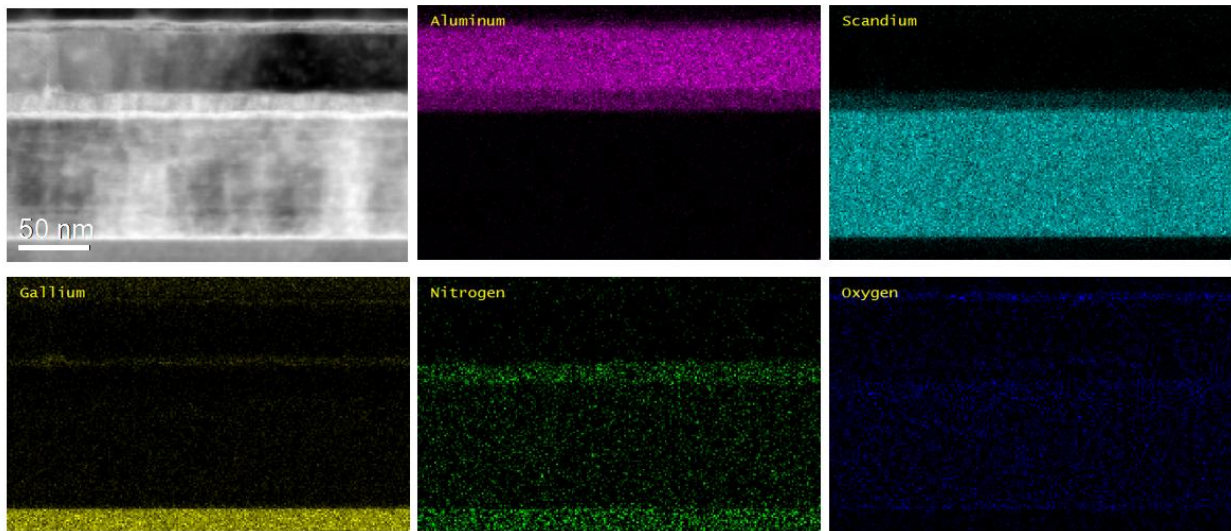


Figure S4. EDS mapping of the TEM cross-section of GaN/Sc/Al_{0.68}Sc_{0.32}N/Al, showing elemental distributions of aluminum, scandium, gallium, nitrogen and oxygen.

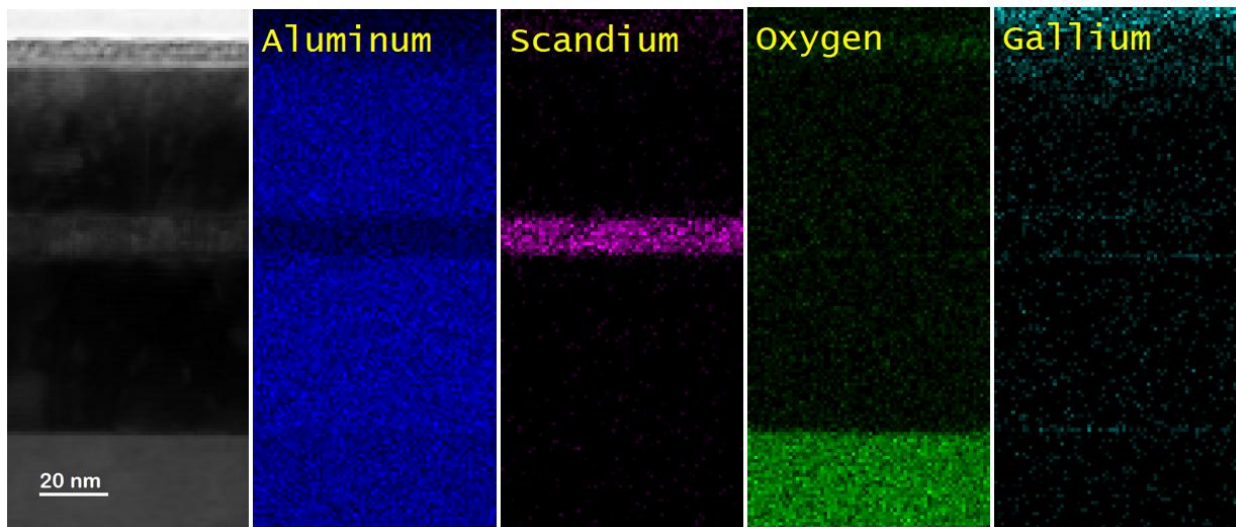


Figure S5. EDS mapping of the TEM cross-section of Sapphire/Al/Al_{0.68}Sc_{0.32}N/Al, showing elemental distributions of aluminum, scandium, gallium, nitrogen and oxygen.

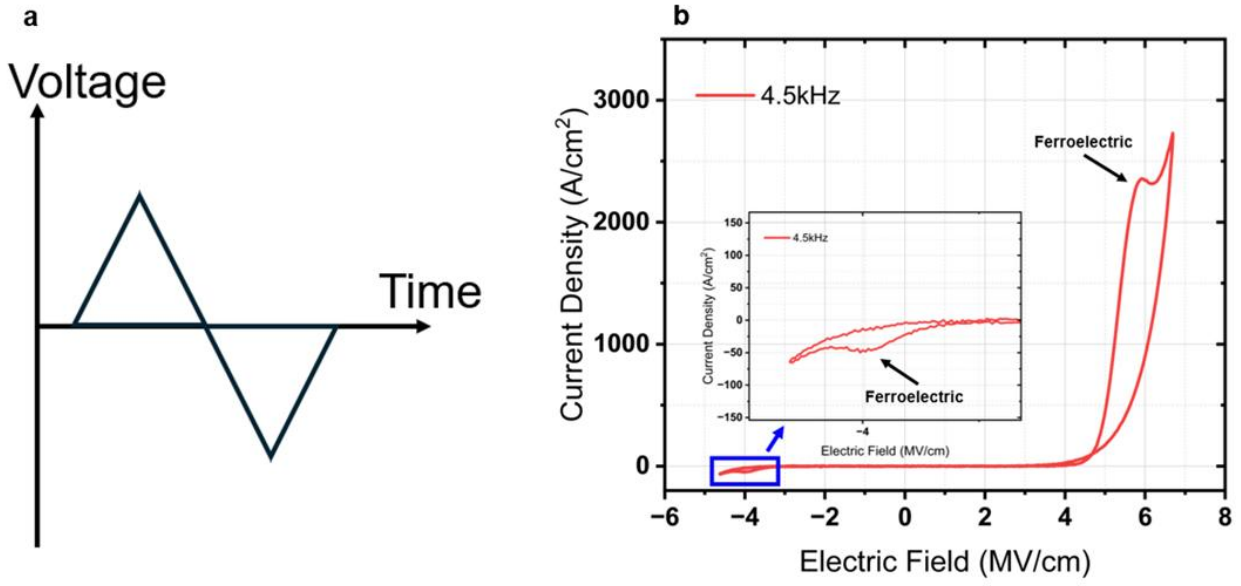


Figure S6. (a) Triangular waveform J-E loop hysteresis loops. (b) Current density vs. electric field of Sc/Al_{0.68}Sc_{0.32}N /Al ferroelectric capacitors under 4.5 kHz, with black arrows pointing to ferroelectric current due to dipole switching. Zoomed-in is the current density behavior at negative applied electric field.

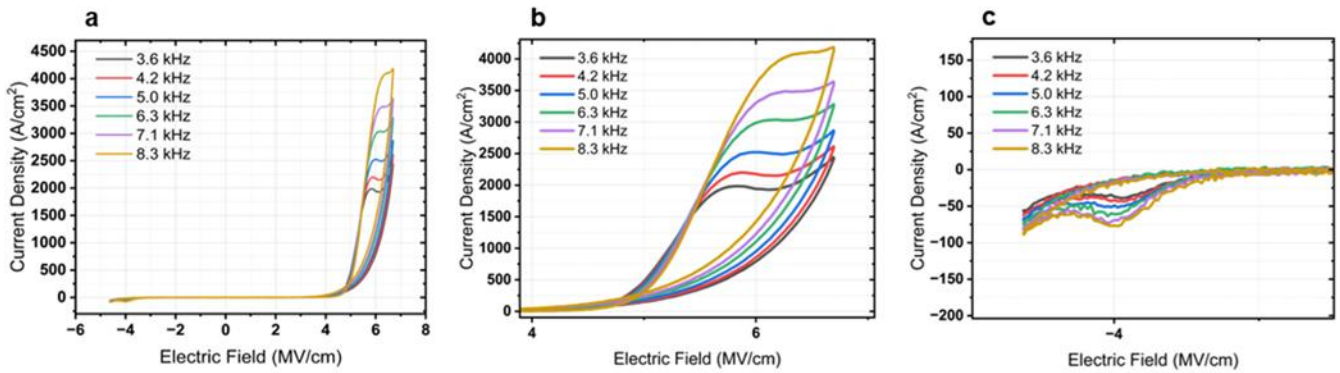


Figure S7. Ferroelectricity vs. frequency under AC I-V test. (a) J-E hysteresis loop of Sc/Al_{0.68}Sc_{0.32}N /Al ferroelectric capacitors under different frequencies. (b) Zoomed-in ferroelectric switching peaks and resistive leakage at positive applied electric fields. (c) Zoomed-in ferroelectric switching and resistive leakage at negative electric fields.

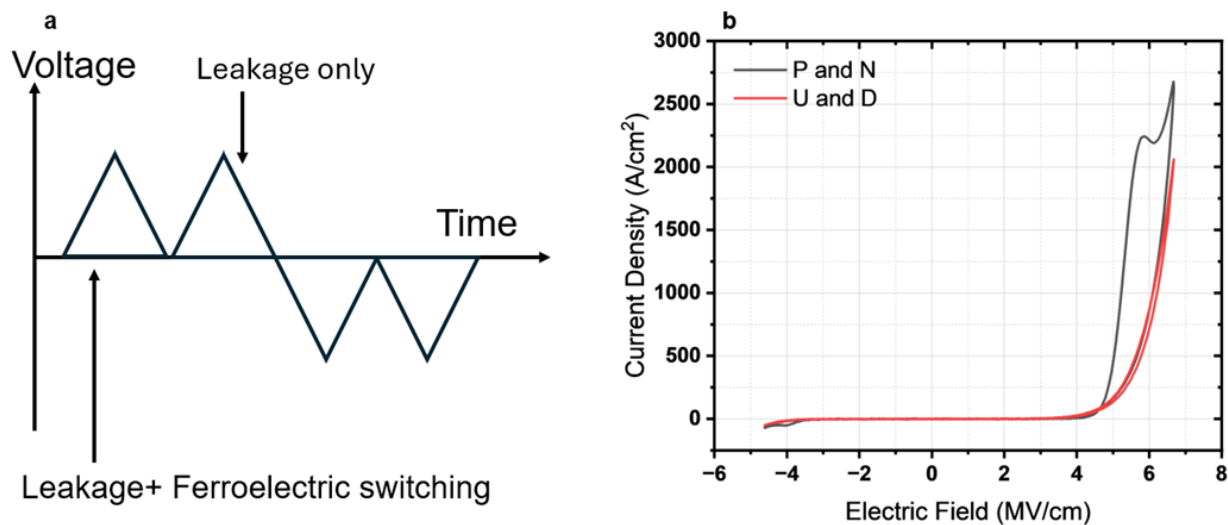


Figure S8. (a) Waveform of triangular PUND J-E test. (b) Triangular PUND J-E hysteresis loops under 4.5 kHz for Sc/Al_{0.68}Sc_{0.32}N/Al capacitors before leakage subtraction.

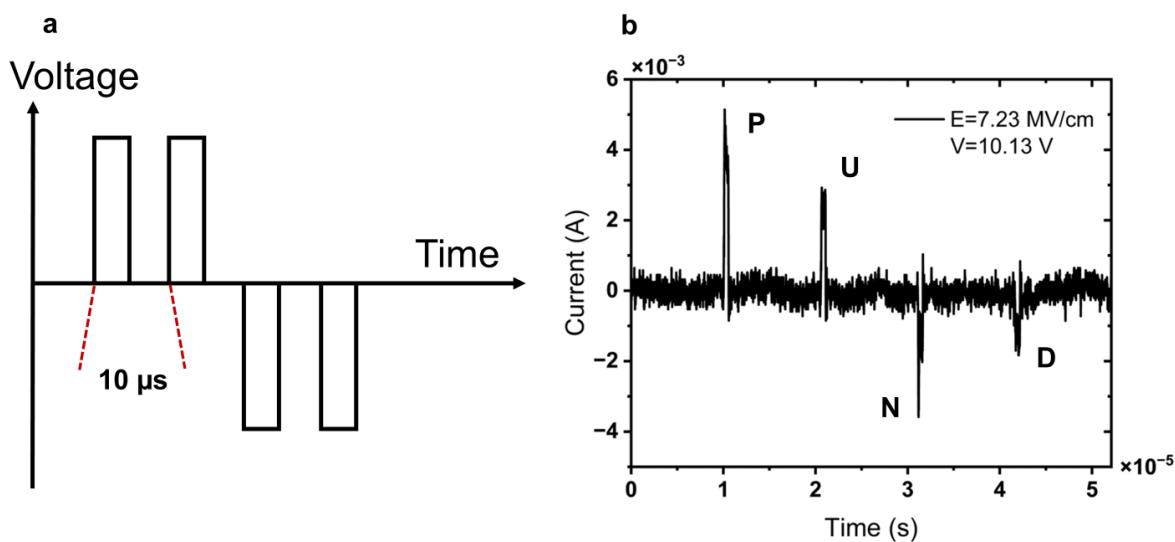


Figure S9. (a) Rectangular waveform of ultra-fast 500 ns PUND measurement. (b) Current-time response of a Sc/Al_{0.68}Sc_{0.32}N/Al capacitor from PUND measurement with an applied voltage of 10.13 V.

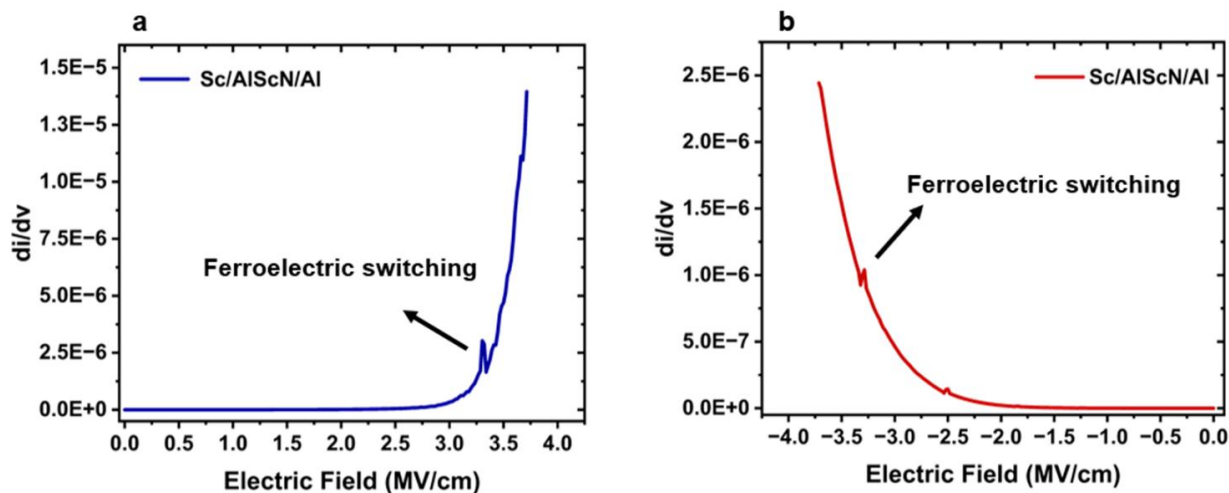


Figure S10. E_C identification from a quasi-DC I-V sweep of a Sc/Al_{0.68}Sc_{0.32}N/Al capacitor. (a) First derivative of current with respect to voltage vs. applied electric field for path 1 in Fig. 2i. (b) First derivative of current with respect to voltage vs. applied electric field for path 3 in Fig. 2i.

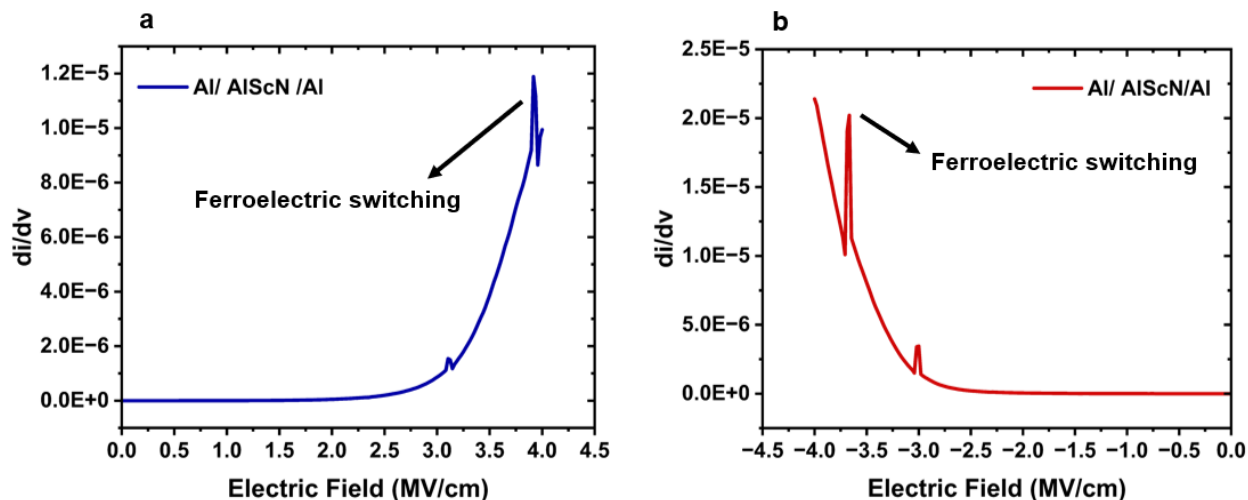


Figure S11. E_C location from a quasi-DC I-V sweep of an Al/Al_{0.68}Sc_{0.32}N/Al capacitor. (a) First derivative of current with respect to voltage vs. applied electric field for path 1 in Fig. 3a. (b) First derivative of current with respect to voltage vs. applied electric field for path 3 in Fig. 3a.

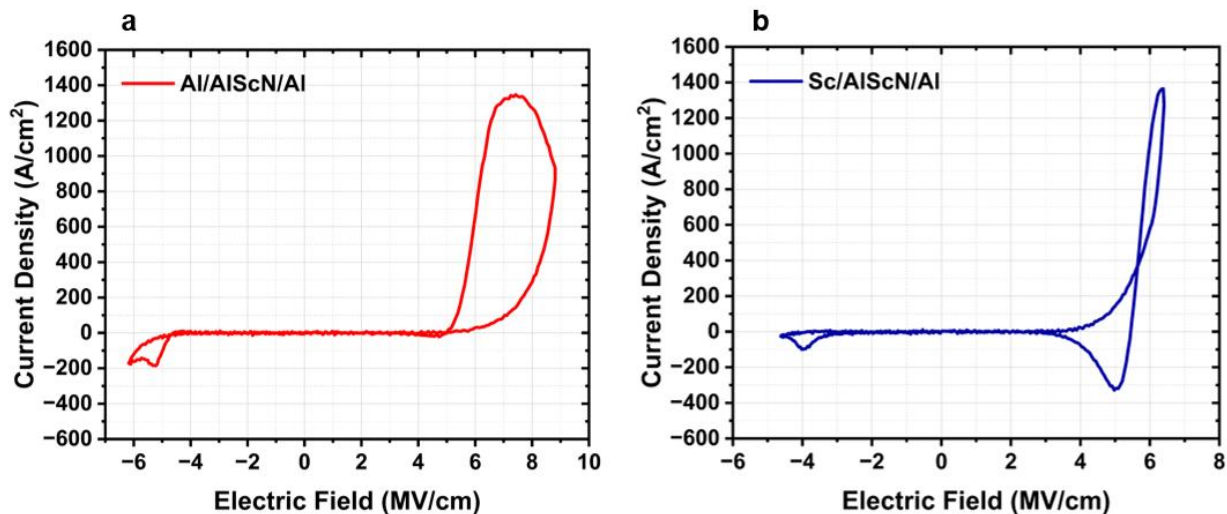


Figure S12. 25 kHz Triangular PUND J-E hysteresis loop with leakage compensation. (a) 8.80 MV/cm to -6.17 MV/cm sweeping loop of an Al/Al_{0.68}Sc_{0.32}N/Al capacitor. (b) 6.40 MV/cm to -4.62 MV/cm sweeping loop of a Sc/Al_{0.68}Sc_{0.32}N/Al capacitor.

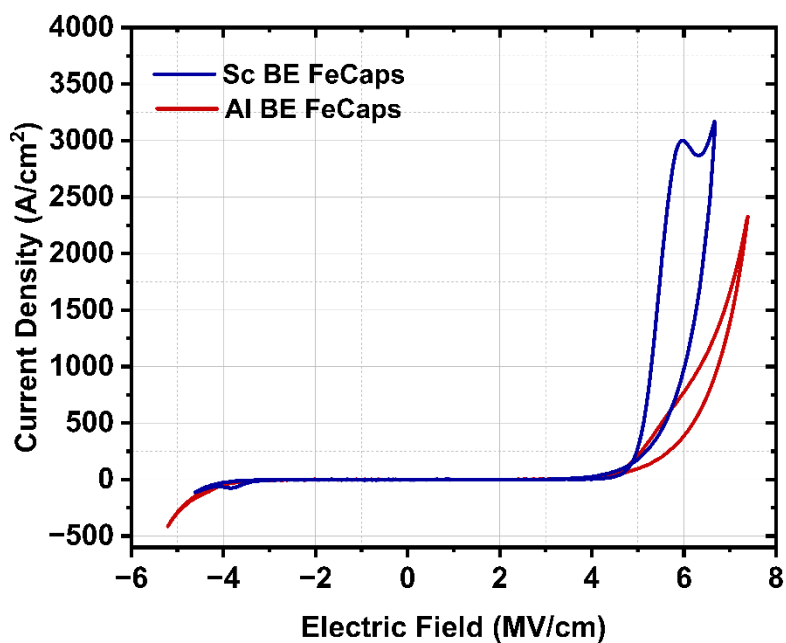


Figure S13. 7.1 kHz Triangular PUND J-E hysteresis loop without leakage compensation of Sc BE FeCaps and Al BE FeCaps, showing the E_{C^+} difference between the two devices.

Bottom Electrode	Log(E ₀)	Standard Deviation (Log(E ₀))	E ₀ (MV/cm)	α	Standard Deviation(α)	R ²
Sc	0.453	± 0.026	2.84	0.036	±0.0063	0.87
Al (low frequency)	0.565	± 0.010	3.60	0.028	±0.0024	0.98
Al (high frequency)	0.262	± 0.071	1.83	0.097	±0.016	0.97

Table S1. Logarithmic fitting of |E_c| and frequency information of FeCaps with different bottom electrodes

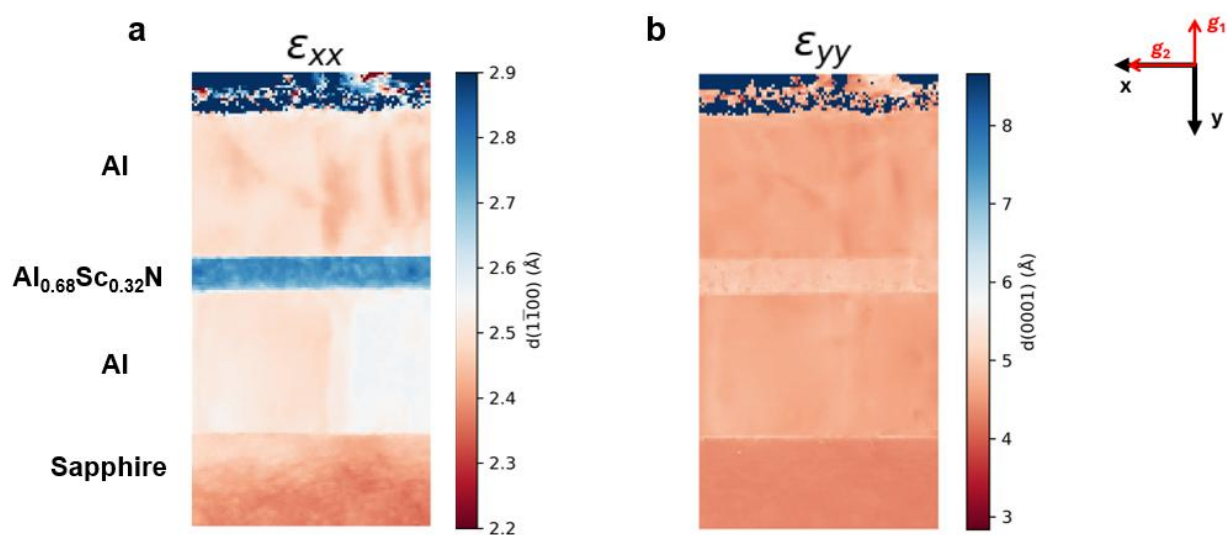


Figure S14. Out-of-plane and in-plane mapping of sapphire/Al/Al_{0.68}Sc_{0.32}N/Al calculated from strain mapping along $[1\bar{1}00]$ of sapphire. (a) In-plane parameter mapping of AlScN. (b) Calculated out-of-plane parameter of AlScN. The lattice parameter map for Al overestimate the plane spacings as the measurements are done with sapphire as a reference.

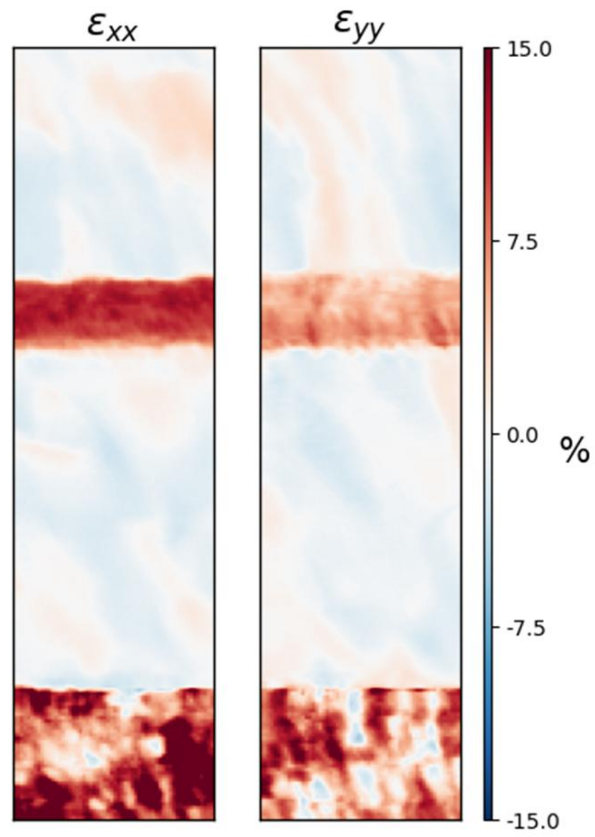


Figure S15. Strain mapping of sapphire/Al/Al_{0.68}Sc_{0.32}N/Al with Al and AlScN symmetrical reciprocal orientation